GEODYNAMIC ORIGIN OF THE COLUMBIA RIVER FLOOD BASALTS

by

JONATHAN PERRY-HOUTS

A DISSERTATION

Presented to the Department of Earth Sciences
and the Graduate School of the University of Oregon
in partial fulfillment of the requirements
for the degree of
Doctor of Philosophy

December 2018

DISSERTATION APPROVAL PAGE

Student: Jonathan Perry-Houts

Title: Geodynamic Origin of the Columbia River Flood Basalts

This dissertation has been accepted and approved in partial fulfillment of the requirements for the Doctor of Philosophy degree in the Department of Earth Sciences by:

Eugene Humphreys	Chair
Leif Karlstrom	Core Member
Thomas Giachetti	Core Member
Benjamin McMorran	Institutional Representative

and

Janet Woodruff-Borden	Vice Provost and Dean of the Graduate School

Original approval signatures are on file with the University of Oregon Graduate School.

Degree awarded December 2018

DISSERTATION ABSTRACT

Jonathan Perry-Houts

Doctor of Philosophy

Department of Earth Sciences

December 2018

Title: Geodynamic Origin of the Columbia River Flood Basalts

Tertiary history of the Pacific Northwest is closely tied to that of the Columbia River Flood Basalt (CRB) events. The region is, geologically, one of the least well understood parts of the continental United States.

Throughout the Neogene, the Columbia Basin and surrounding terrains appear to have been shaped not by horizontal tectonic forces, but by deep dynamic forcing, driving apparent "vertical tectonics." This class of phenomena appears to be at odds with the traditional tenets of plate tectonics, and yet may prove to be ubiquitous geologic processes worldwide. Many of the processes described here are unique to volcanically-active regions, such as those affected by CRB eruptions and deposition.

In the following chapters I will discuss several physical mechanisms by which lithosphere can deform in the absence of horizontal tectonic stress. These include analyses of the mechanisms associated with metamorphic densification, rheologic transformation owing to magmatic intrusions, and the dynamics of lithospheric delamination.

All code and documentation to reproduce the results presented here can be found in the supplemental files included with this dissertation. Appendices A and B document the purpose, usage, and functionality of each supplementary file.

This dissertation includes previously published and unpublished coauthored material.

CURRICULUM VITAE

NAME OF AUTHOR: Jonathan Perry-Houts

GRADUATE AND UNDERGRADUATE SCHOOLS ATTENDED:

University of Oregon, Eugene, OR, USA
Lewis & Clark College, Portland, OR, USA

DEGREES AWARDED:

Doctor of Philosophy in Geological Sciences, 2018, University of Oregon
Bachelor of Arts in Physics, Minor: Computer Science, 2011, Lewis & Clark College

AREAS OF SPECIAL INTEREST:

Geodynamics
Western U.S. Tectonics
STEM education

PROFESSIONAL EXPERIENCE:

Graduate Employee, University of Oregon, 2012–2018
Student Assistant, Lawrence Berkeley National Lab, 2009–2012

GRANTS, AWARDS AND HONORS:

Advanced certificate of completion, Teaching Effectiveness Program: Graduate Teaching Initiative, University of Oregon, 2018.
Collaborative Research: An integrated mantle to surface study of the causes and consequences of high topography in the Northern US Cordillera, NSF EAR-1727046/1727139/1727451, 2017.
Outstanding TA Award, Department of Earth Sciences, University of Oregon, 2017.
Departmental Honors, Department of Physics, Lewis & Clark College, 2011.
Feynman Prize, Department of Physics, Lewis & Clark College, 2009.

PUBLICATIONS:

Perry-Houts, J., & Karlstrom, L. (2019). Anisotropic viscosity and time-evolving lithospheric instabilities due to aligned igneous intrusions. *Geophysical Journal International*, 216(2): 791–799. doi: 10.1093/gji/ggy466

Perry-Houts, J., & Humphreys, E. (2018). Eclogite-driven subsidence of the Columbia Basin (Washington State, USA) caused by deposition of Columbia River Basalt. *Geology*, 46(7): 651–654. doi: 10.1130/G40328.1

Humphreys, E., Schmandt, B., Bezada, M., Perry-Houts, J. (2015). Recent craton growth by slab stacking beneath Wyoming. *Earth and Planetary Science Letters*, 429(2015): 170–180. doi: 10.1016/j.epsl.2015.07.066

ACKNOWLEDGEMENTS

The ideas presented here were developed and refined through countless constructive discussions with friends, and members of the Department of Earth Sciences. In particular, I'd like to thank my partner, Hannah Green, and my roommates: Ben Heath, Dylan Colón, Allan Lerner, Dana Reuter, Win McLaughlin, and Mitch Hilbert.

The following chapters are collaborative works, completed with my advisers, Gene Humphreys, and Leif Karlstrom. I'd like to thank them both for their dedication to quality, and the work they contributed to make this document what it is. Peer reviews and edits from Claire Currie, Vic Camp, James Schmitt, Lars Hansen, James Hammond, Juan Carlos Afonso, and an anonymous reviewer all improved the quality and clarity of this work.

Finally, I'd like to thank the developers and contributors to the ASPECT project, as well as the Computational Infrastructure for Geodynamics (CIG; https://geodynamics.org) for building and fostering a supportive geodynamic community. CIG is funded by NSF grants EAR-0949446 and EAR-1550901.

This research was supported in large part by NSF grant EAR-1727451.

TABLE OF CONTENTS

LIST OF FIGURES

Figure Page

LIST OF TABLES

Table Page

CHAPTER I

INTRODUCTION

This dissertation represents a body of research focused on understanding the physical origin of geologic features in the Pacific Northwest. It is primarily concerned with events surrounding the Miocene Columbia River Flood Basalt (CRB) events. To this end, I will discuss several aspects of CRB eruption mechanisms, and consequences of their deposition.

In Chapter II, I discuss the consequences of rapidly depositing dense rock above a basaltic crust. I will demonstrate a feedback mechanism driven by syn-depositional metamorphism in the lower crust caused by increased lithostatic load. This work was coauthored with Gene Humphreys, and is published in volume 46 of the journal *Geology*.

Chapter III shifts localities to the CRB's eruptive origin, the Chief Joseph Dike Swarm. In it, I discuss the origin of the unusual topographic structure centered on the Wallowa Mountains, and surrounding terrain. This chapter is a work in progress, and represents our current understanding of the geodynamic history of the Wallowa area. As such, we can draw robust conclusions from our geodynamics models, but they have missing components that render them inadequate for further reaching interpretations. The text is also somewhat rough, and still in preparation for publication. This work results from many years of discussions with Gene Humphreys, and others. Gene is a coauthor on the in-prep publication.

Finally, in Chapter IV, I discuss the consequences of igneous intrusions on bulk rheology of the lithosphere. I present simple analytic models for the viscous anisotropy that results from aligned intrusions, when the intrusions have contrasting viscosity to the host rock. I then show a series of numerical models

which test the net effect of such a rheologic structure on the stability of mantle lithosphere. This chapter was coauthored with Leif Karlstrom, and is in press at *Geophysical Journal International*.

CHAPTER II

ECLOGITE-DRIVEN SUBSIDENCE OF THE COLUMBIA BASIN (WASHINGTON STATE, USA) CAUSED BY DEPOSITION OF COLUMBIA RIVER BASALT

From Perry-Houts, J., & Humphreys, E. (2018). Eclogite-driven subsidence of the Columbia Basin (Washington State, USA) caused by deposition of Columbia River Basalt. *Geology*, 46(7). https://doi.org/10.1130/G40328.1. The ideas presented in this chapter came from discussions with Gene Humphreys. Gene provided scientific insight, and lots of text edits. I developed and implemented the models, and wrote most of the text.

2.1 Summary

The south-central portion of the Columbia Basin in Washington State, although not the primary eruptive center for the Columbia River Basalt (CRB), contains the thickest package of CRB lavas at over 4 km. Prior to CRB deposition, the region was a sediment-filled rift basin dating back to the early Eocene. Previous studies interpret a lower-crust high velocity body below the thick basalt deposits as a syn-extensional magmatic underplate. CRB layers thicken toward the center of the basin, revealing a pulse of subsidence during deposition that ceased coincident with cessation of CRB eruptions. We propose a subsidence mechanism based on metamorphic transition of the underplate from basalt to eclogite facies, driven by the increased pressure of CRB loading. We demonstrate the plausibility of our interpretation using numerical models of the mechanical and chemical components of the system. Further, we constrain the effective elastic thickness of the Miocene Columbia Basin lithosphere, finding it to be much thinner (5–10 km) than previous estimates.

2.2 Introduction

The Columbia River Flood Basalt (CRB) erupted ~17–6 Ma from NE Oregon and adjacent portions of Idaho and Washington (Fig. 2.1). These flows covered the Columbia Basin as nearly flat, self-leveling, inflation flows. Basalt accumulation was greatest not near the primary source of eruption, but in the center of the Columbia Basin (Fig. 2.1), where over 4 km of CRB ponded (Reidel et al., 1989). As evidenced by the CRB flows thickening toward the center of the basin (Fig. 2.2), progressive basin subsidence occurred during CRB activity, deepening a depression that CRB flows repeatedly filled and over-topped. Subsidence ended with the cessation of CRB deposition, and the region has not experienced significant subsidence since (Reidel, Camp, Tolan, & Martin, 2013). We use the name central Columbia Basin downwarp (CCBD) to refer to the region of subsidence roughly outlined by the 2 km CRB isopach in Figure 2.1.

2.3 Geologic Context

Basic aspects of crustal structure in the greater Columbia Basin region are represented in Figures 2.1 and 2.2. A major phase of regional extension and volcanism occurred during the ca. 53 Ma accretion of Siletzia, accompanied by an outward stepping of subduction and establishment of the present Cascadia subduction zone (Christiansen & Yeats, 1992). Regional extension includes the creation of large core complexes in NE Washington and trans-tensional basins now exposed along the eastern flank of the north Cascades uplift. The Swauk and Chiwaukum basins (Fig. 2.1) preserve the most complete record of sedimentation. They are filled with Eocene sediments and volcanic rocks ranging in age from ~55–40 Ma (Taylor, Johnson, Fraser, & Roberts, 1988). These basins trend SE into the CCBD, where they are covered by CRB flows. Drill holes through the

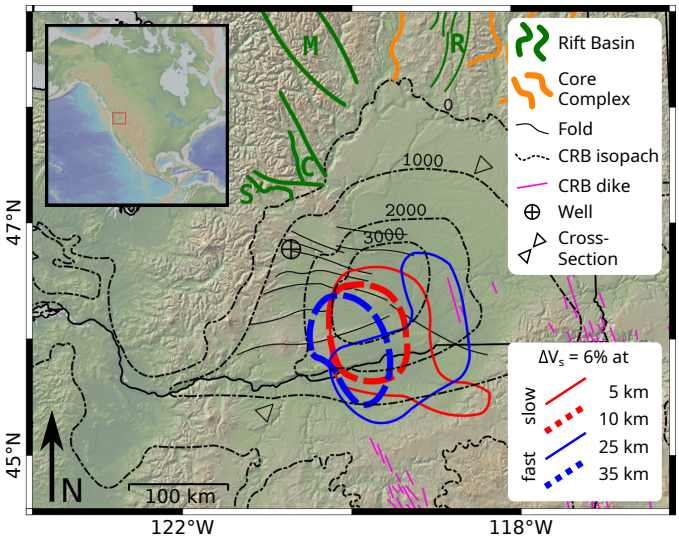

Figure 2.1. Map showing features that correlate with the central Columbia Basin downwarp. Accumulated thickness of the CRB flows is indicated with black dashed lines (thickness in meters). CRB ponding filled the downwarp, which subsided during the CRB eruptions. Subsidence centered on an Eocene rift basin associated with coeval core complex and trans-tensional basin activity in northern Washington. The Swauk (S), Chiwaukum (C), Republic (R), and Methow (M) grabens are labeled. The rift basin is imaged with active-source seismology along the cross section (indicated with triangles) (Catchings and Mooney (1988);Fig. 2.2) and with surface waves (Gao, Humphreys, Yao, & van der Hilst, 2011). The anomalous crustal structure imaged in the immediate vicinity of the downwarp includes 5–6 km of sediment beneath ~4km of CRB, and ~16 km of high-velocity lowermost crust interpreted by Catchings and Mooney (1988) to be rift-related magmatic underplate. Red and blue lines outline areas of low- and high-velocity crust (Gao et al., 2011). Topography adapted from GMRT synthesis (Ryan et al., 2009).

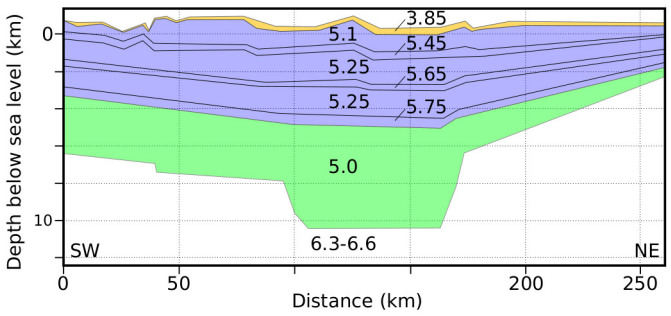

Figure 2.2. The upper crust along the cross section indicated in Figure 2.1, after Catchings and Mooney (1988). Numbers on plot give the P-wave velocity in km/s. Tan = post-Columbia River Basalt (CRB) sediment. Blue = CRB flows. Green = Eocene sediment. White = basement. Note the deep sediment-filled rift basin, and CRB flows thickening toward the basin center, indicating that the basin subsided during deposition, and not after.

CCBD penetrate these same Eocene sedimentary units (Campbell, 1989). The formation ages of the early Swauk, Chiwaukum, and (where resolved) Eocene rift basin in the CCBD are similar to the unroofing of nearby core complex (54–47 Ma, Kruckenberg, Whitney, Teyssier, Fanning, and Dunlap (2008)) and vigorous regional volcanism (Christiansen & Yeats, 1992; Gaschnig, Vervoort, Lewis, & McClelland, 2010).

The active source seismic study of Catchings and Mooney (1988) and the surface wave and receiver function study of Gao et al. (2011) provide images of the deep structure in the CCBD and surrounding area. Eocene sediments in the CCBD locally extend to ~11 km beneath the surface, defining a deep, local (~110 × 80 km), rift structure. Immediately below the area of deep sediment accumulation, and of similar horizontal dimensions, is an anomalous region of seismically high velocity (V_P = 7.5 km/s) lower crust extending from ~23 km to ~40 km depth (Fig. 2.1). We assume this to be the basaltic underplate portion of the rift structure, as proposed by Catchings and Mooney (1988), with the 40 km seismic Moho representing local basalt-eclogite coexistence pressure, and

underlying root seismically indistinguishable from surrounding mantle. The crustal section from 11 km–23 km has been interpreted as either crystalline North America (Catchings & Mooney, 1988) or Farallon slab connected at depth to Siletzia (Gao et al., 2011). Either interpretation is consistent with our modeling.

2.4 Eclogite-Driven Subsidence

The rate and magnitude of Miocene subsidence in south-central Washington is far greater than any other CRB depocenter, at up to 10 mm/yr throughout Grande Ronde deposition (Reidel et al., 2013). Because this time period does not coincide with any major change in regional tectonics (Christiansen & Yeats, 1992), we infer subsidence was driven by local vertical forcing rather than far-field horizontal tectonics.

2.4.1 Isostasy and Flexure

The core logic of our model is a simple isostatic argument. Loading from CRB deposition increases lithostatic pressure throughout the crust, pushing lower-crustal basaltic rocks across the phase transition to eclogite facies. As rocks metamorphose from basalt to eclogite they densify, contracting the crust and creating a topographic low relative to a column that did not eclogitize. The resulting depression traps subsequent lava flows, compounding the effect over time.

Conceptually, we model the mechanical aspects of this system in two distinct steps. First, when a new basalt flow is deposited, we assume that its weight is transmitted hydrostatically to the lower crust. This implies that an equal volume of lower crust is eclogitized, directly below the new deposit.

Mechanical contraction is filtered by the elastic strength of the plate, producing a smoothed topographic response. We model this effect as an equivalent

load applied to an isostatically-supported elastic plate. We use a thin-plate assumption (Turcotte & Schubert, 2014), for which the dominant forces are buoyancy, and elastic bending stress, as expressed by the equation

$$\nabla^2 D \nabla^2 \, w(x,y) + [\rho_m - \rho_b] \, g \, w(x,y) = L(x,y), \tag{2.1}$$

where w is displacement as a function of position, (x,y); ρ_b and ρ_m are respectively density of basalt and mantle; L is vertical loading stress; and D is flexural rigidity. Flexural rigidity is defined as

$$D = \frac{E T_e^3}{12(1-\nu^2)}, \tag{2.2}$$

where E is Young's Modulus, T_e is effective elastic thickness, and ν is Poisson's ratio.

We numerically solve Equation 2.1 with the finite difference method. We initialize our model with a small topographic depression, representing the Eocene basin just prior to CRB onset, which we take to be in isostatic equilibrium. Assuming that an equal volume of lower-crustal basalt eclogitizes upon deposition, we expect a proportional reduction in crustal volume.

We use reference densities 3000, 3300 and 3370 $\mathrm{kg\,m^{-3}}$ for basalt, mantle, and eclogite, respectively to calculate the effective load of eclogitization. We assume an elastic plate with Young's modulus 7×10^{10} Pa, and Poisson's ratio 0.25. Each time step represents a lava flow filling the existing depression, and the crustal downwarping caused by the newly formed eclogite load. Each event adds a proportional volume of eclogite to the root structure, for a cumulative root growth proportional to cumulative deposition.

Our calculations assume the system reaches isostatic equilibrium between lava flows, and omits dynamic effects such as mantle convection and lateral crustal flow, which may affect the long-term evolution of the system (H. Wang & Currie, 2017).

The nature of Equation 2.1 results in a smooth subsidence response, making the model relatively insensitive to the detailed shape of the initial basin. For the models presented in Figure 2.3, our initial geometry is a radial Gaussian function with RMS width of 15 km and depth of 50 m. Any short-wavelength load excites the natural bending wavelength of the crust. If the initial basin is much wider than the natural bending wavelength, the basin localizes to the natural bending wavelength with repeated lava flows. A deeper initial basin results in faster basin development. The long-term resulting structure is qualitatively the same in all cases. Model results are shown in Figure 2.3, and further details of our methods can be found in Appendix A.

Based on our modeling, the observed basin geometry is possible only if the crust has an effective elastic thickness between 5–10 km. This differs from the 25–35 km estimate of Lowry and Pérez-Gussinyé (2011), which is based on the ratio of topography to Bouguer gravity. We think the discrepancy in estimated effective elastic thickness is a consequence of topographic flattening created by the CRB deposits.

2.4.2 Reaction Kinetics

Although we describe our flexural model as an iteration over individual lava flows, it makes no predictions of the actual time elapsed between steps. Rather, each model step represents time taken for the slowest physical process in the system to act. In the following paragraphs we show that neither reaction processes, nor latent heat release hinders the basalt to eclogite transition on scales relevant to eclogite-driven subsidence. Therefore, we conclude that the duration of the CRB deposition is the limiting mechanism for this system. That is, by the time each new flow begins, metamorphism owing to the previous flow has come to equilibrium.

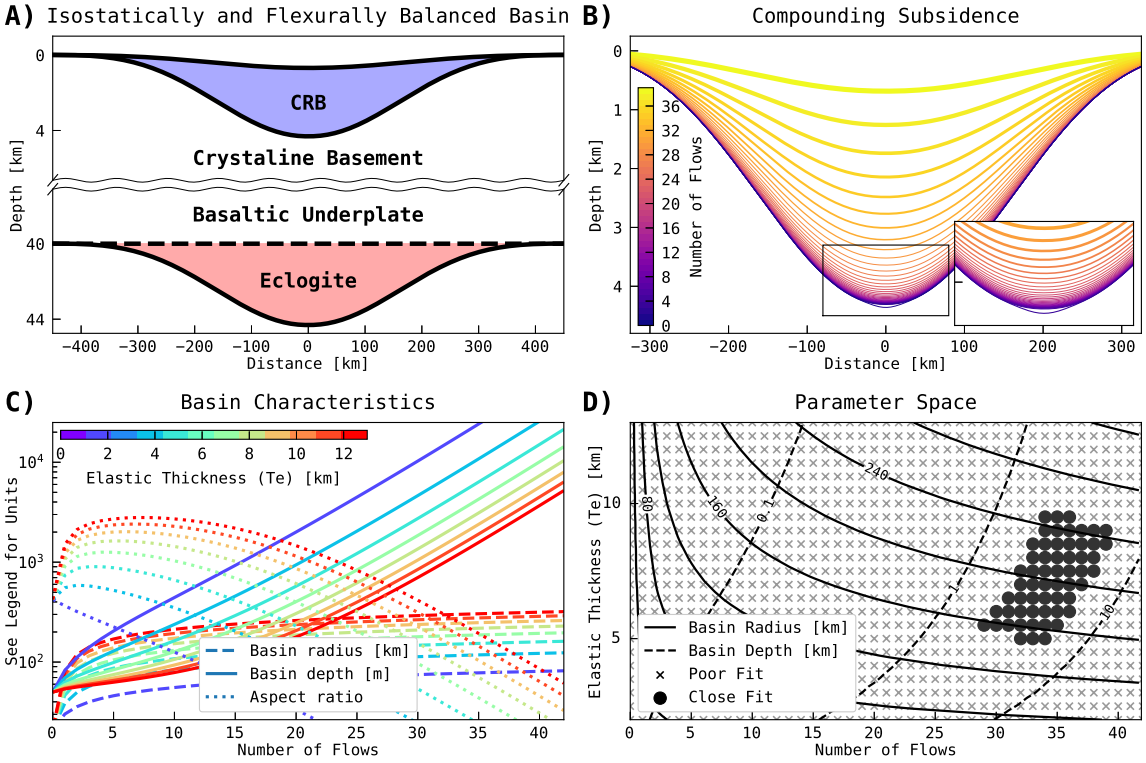

Figure 2.3. Models of time-evolving eclogite loading on an isostatically-supported elastic plate. A: Beginning with a small depocenter, a larger basin develops by repeatedly filling the existing topography and calculating new subsidence owing to lower-crustal eclogite formation. B: Depositional interfaces over time, illustrating the compounding effect of the eclogitization subsidence mechanism. Each flow is deposited as a flat layer filling the previous depression, and subsequently downwarps as a result of newly generated eclogite. Color represents the sequence of deposition. Line thickness is proportional to the thickness of the basalt layer. Inset shows zoom-in of initial topography. C: Basin geometry characteristics over time for varying elastic plate thicknesses. Other parameters are held constant across models. Basin depth increases slowly at first, and accelerates as the basin size, and hence load, increases. Basin radius rapidly adjusts to reflect the plate's natural flexural wavelength. Aspect ratio (radius/depth) reveals that in this adjustment stage, radial growth briefly out-paces deepening. Long-term basin growth is dominated by deepening. D: The effects demonstrated in (C) trade off differently for different elastic plate thicknesses. Contours denote basin depth and radius over time for different plate thicknesses. Models whose geometries are similar to the Columbia Basin are plotted in filled circles, setting narrow limits on possible Miocene plate thickness.

Previous studies on the basalt to eclogite transition have found that eclogitization takes place on geologically relevant time scales at temperatures above 400–600 °C in dry basalt (Ahrens & Schubert, 1975; Ito & Kennedy, 1971), although dry gabbroic facies may remain metastable for substantial time, even at high temperatures (Hacker, 2013). However, the same reactions progress rapidly to stable equilibrium in the presence of small amounts of water (Ahrens & Schubert, 1975; Hacker, 2013), as we expect to exist in abundance in the Cascadia backarc. Hence we assume the lower crust of the Columbia Basin is capable of reacting quickly and completely from basalt to eclogite upon local changes in pressure and temperature.

The latent heat of reaction inhibits eclogitization. As this heat diffuses away, the reaction can continue. The following analysis shows the release of latent heat has negligible effect on the reactions we consider. Following O'Connell and Wasserburg (1972), we consider a vertical thermo-chemical profile through the crust. The deposition of lava both advects the geotherm down with the sinking crust, and causes the release of latent heat at depth. This modified geotherm then conductively cools back toward its original equilibrium slope.

We model the thermo-chemical system with a heat conservation equation and an Arrhenius reaction equation, respectively:

$$\rho C_p \left(\frac{\partial T}{\partial t} + u \cdot \nabla T \right) - \nabla \cdot (\rho C_p \alpha \nabla T) = \rho T \Delta S \left(\frac{\partial X}{\partial t} + u \cdot \nabla X \right), \tag{2.3}$$

and

$$\frac{\partial X}{\partial t} = A \exp\left(\frac{-E_a}{RT} \right) \left\{ \frac{1}{2} \left(1 + \tanh\left(\frac{P - P_c}{\delta_p} \right) \right) - X \right\}, \tag{2.4}$$

where T is temperature, u is deposition rate, P is pressure, P_c is facies coexistence pressure as a function of temperature, X is fraction eclogite facies, ρ is density, C_p is specific heat capacity, α is thermal diffusivity, ΔS is specific entropy change of eclogitization, E_a is activation energy of reaction, R is the universal gas constant,

δ_p is a smoothing factor for the coexistence boundary as a function of pressure, and A is an Arrhenius coefficient.

We non-dimensionalize Equations 2.3 and 2.4 using a modified Péclet number for chemically reactive continuum,

$$Pe_r = \frac{\mathbf{U}^3}{\mathbf{SG}\alpha}, \tag{2.5}$$

where $\mathbf{G}$ is a reference geothermal gradient, and other boldface variables are representative values of variables in Equation 2.3. Finite element solutions to Equations 3 and 4, and instructions for reproduction, are provided in the supplemental files provided with this dissertation. However, one can easily verify that, for any geological system, $Pe_r << 1$. Therefore, the system tends toward the limiting case of instantaneous thermal diffusion, implying that latent heat has negligible effect on this system.

2.5 Discussion

Eclogitization has been discussed before as a driver of localized dynamic topography. A model similar to the one presented here has been proposed for sediment-loaded intracratonic basins (Hamdani, Mareschal, & Arkani-Hamed, 1994; Naimark & Ismail-Zadeh, 1995), where eclogitization is driven primarily by a cooling geotherm, and surface loading is of secondary importance. Compressional tectonics may also drive eclogitization, forming basins like the East Barents Sea (Gac, Huismans, Simon, Podladchikov, & Faleide, 2013), and affecting the buoyancy structure of aging mountain belts (Fischer, 2002).

The minimum requirement for eclogite-driven subsidence is the presence of basaltic lower crust. Rift structures are common localities for lower crustal magmatic underplates. The CCBD, and intracratonic basins mentioned above

all have rift histories. However, lower crustal gabbro may also form in significant quantities in other settings, such as at arcs and hot spots.

Additional lower crustal density owing to eclogitization could be a precursor to lithospheric delamination, and associated lithospheric recycling, uplift, and volcanism (Krystopowicz & Currie, 2013). It is noteworthy that the mechanisms discussed here are examples of so-called vertical tectonics, driven not by far-field horizontal forces, but by localized changes in lithospheric buoyancy. This class of tectonic processes appears to be a significant driver of tectonic evolution from the local and concentrated scale of the CCBD, to uplift of the entire North American Cordillera.

2.6 Conclusion

The occurrence of a local downwarp occurring only during the short duration of CRB deposition, and at the site of an apparent earlier magmatic underplate, strongly suggests the event was driven by creation of a local load on the crust. With simple numerical models of the physical and chemical components of the system, and inferring from the pre-Miocene geology a basaltic lower crust straddling the basalt-eclogite transition, we show that formation of lower-crustal eclogite during CRB loading would drive localized subsidence in a manner consistent with the modern Columbia Basin geometry and structure. We can think of no other satisfactory explanations for the anomalous, localized Miocene subsidence of the central Columbia Basin. Further, our models constrain the effective elastic thickness of the Miocene Columbia Basin crust to under 10 km.

Our study supports the hypothesis, proposed by others, that similar mechanisms may explain other localities of anomalous subsidence. In general, lower-crustal eclogitization is capable of producing deep basins without far-field

tectonic driving, and may be responsible for anomalous topographic features globally.

2.7 Bridge

Here we have proposed a geodynamic origin for the anomalously thick CRB deposits in the Central Columbia Basin. Our interpretation involves densification of the lower crust, and the isostatic response of its tectonic plate to the added load. We propose that metamorphic densification produced a localized depression in the crust, but claim that the tectonic plate remained structurally in-tact. In similar density-stratified systems, the dense underplate may eventually founder into the mantle, releasing its vertical traction on the overlying plate, and producing localized uplift. The following chapter will explore the consequences of lower crustal density structure on topographic history of the Wallowa Mountains area, associated with the coeval eruption of the CRB's.

CHAPTER III

A GEODYNAMIC ORIGIN FOR UNUSUAL RADIAL TOPOGRAPHY OF THE WALLOWA MOUNTAINS, (OREGON, USA)

This chapter represents a status update on work that is in-progress. The concepts presented here are well-developed, and the preliminary model results are robust (subject to limitations discussed in Section 3.6), but the text remains rough in many places, and has not been subject to peer review. I am performing this work in collaboration with Gene Humphreys. Gene is a coauthor on the in-prep article based on this work, and has contributed substantial scientific insight throughout the process.

3.1 Summary

The Wallowa Mountains of northeastern Oregon stand apart from the surrounding terrain. Isolated by a moat-like valley, the Wallowas are encirled by a concentric ring of the highest mountains in the area. The regional topography forms a distinctive 'bullseye' pattern.

The area is also notable as the primary exposure of the Chief Joseph Dike Swarm, and dominant eruptive origin of the voluminous Grande Ronde member of the Columbia River Flood Basalts (CRB). Grande Ronde lava flows cover the landscape, extending to the Pacific Ocean in some places, but primarily deposited in the central Columbia Basin of south-central Washington.

Some aspects of the area's post-Miocene tectonic history are relatively well understood. It has been commonly suggested that the central Wallowa mountains uplifted as an isostatic response to the loss of a dense garnet-rich root. However, the origin of the moat, and the circumfrential bulge, have never been adequately addressed.

Several lines of evidence lead us to propose that the complete bullseye structure originally formed as a regional plateau, into which the moat later subsided. We suggest that the initial phase of uplift was caused by crustal inflation, as CRB magmatic sills propagated through the mid-crust. Magma that was generated and stored in reservoirs to the south and east appears to have been forced laterally by stresses of a delaminating flat slab fragment, and by the weight of dense plutonic roots in the lower crust.

To support our hypothesis, we have developed a set of numerical models in which we test the pausibility of deep dynamic tractions generating and steering magmatic sills. We use an approximation for independent melt transport, coupled with a compressible viscous crust and mantle deformation. Our models support the possibility of such a mechanism to direct melt movement within the crust, and to generate substantial uplift by crustal inflation.

3.2 Introduction

The bullseye topography centered on the Wallowa Mountains of northeast Oregon has been described previously by several workers. It has frequently been used as evidence of local delamination, usually in the context of dense pluton root foundering. However, an origin for the surrounding moat, and circumferential mountain ring, have never been adequately addressed.

The observed correlation between bullseye formation and CRB eruptions, in both time and space, leads us to look for connections between the two events. Geologic evidence reveals the sequence of deformations that led to the current topographic signature. Specifically, we interpret from the geologic record that the moat subsided into an existing plateau, completing the bullseye as a late-stage feature.

We suggest that the moat formation can be explained with mechanisms described by H. Wang and Currie (2017). In this work we aim to find the mechanism responsible for the initial plateau formation. We use several acronyms for regional features which are defined graphically in Figure 3.1.

3.3 Background

3.3.1 Tectonic Origin

The Wallowa Mountains stand at the northeast end of the Blue Mountain Province (BMP), an amalgamation of Paleozoic-Mesozoic island arcs that accreted to North America around the latitude of northern Nevada during the late Triassic to early Jurassic (Dorsey & LaMaskin, 2008; Schwartz et al., 2011). The BMP was transported northward to its present location in the Cretaceous, along a large dextral strike-slip fault system (Wyld & Wright, 2001).

The modern Wallowa range is centered on a granitic batholith, intruded into the BMP in the Cretaceous (Kays, Stimac, & Goebel, 2006). O'Driscoll and Johnson (2008) found geochemical indicators that, during formation, the Wallowa Batholith (WB) fractionally crystallized a dense garnet-rich root.

The BMP remained volcanically quiescent through the Paleogene, unaffected by the vigorous post-orogenic volcanism of the nearby Ignimbrite Flareup (Christiansen & Yeats, 1992). We take the Ignimbrite Flareup to be evidence of flat slab removal (Farmer, Bailley, & Elkins-Tanton, 2008; Humphreys, 1995), implying that the BMP's relative quiescence shows Farallon slab remained locally attached. Quiescence lasted until the Miocene, when Columbia River Flood Basalt dikes intruded the region, erupting most CRB lava through the Wallowa Batholith and surrounding area (Barry et al., 2013).

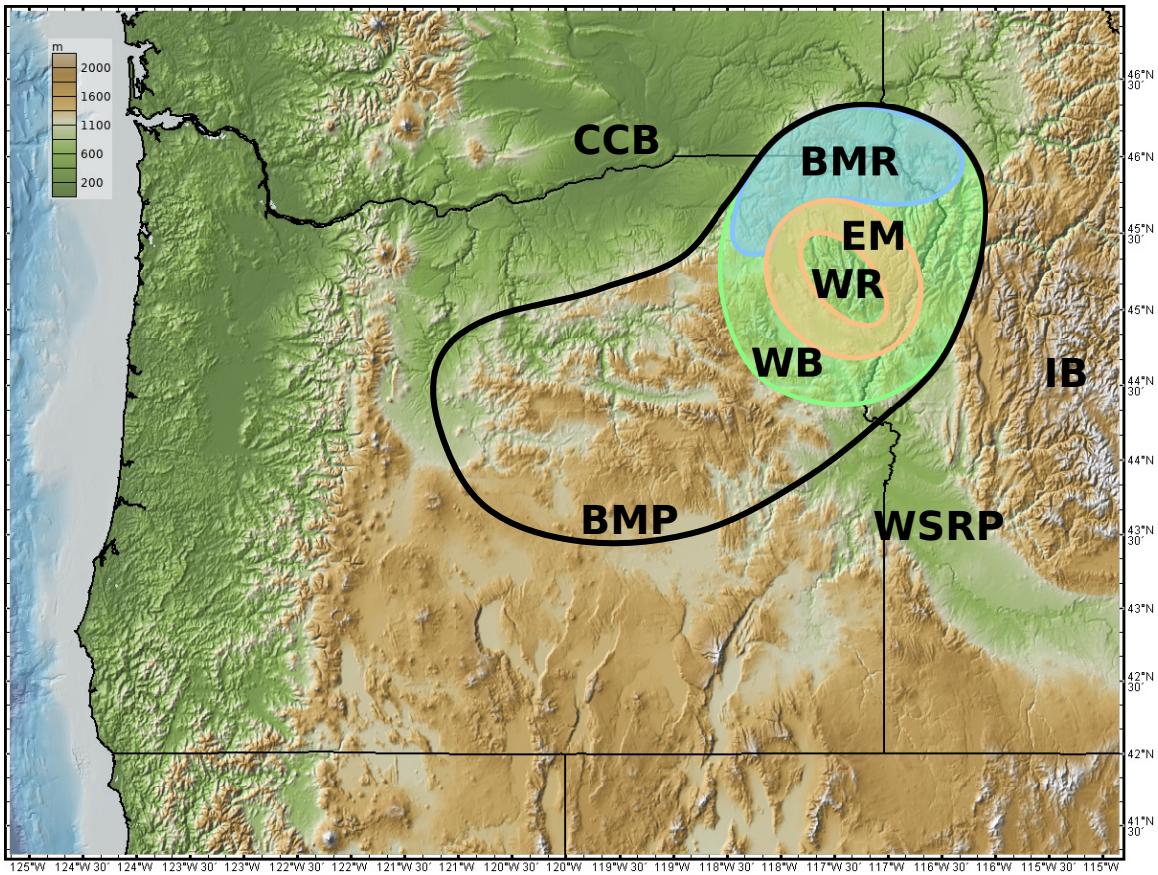

Figure 3.1. Map showing key features of the Wallowa Mountains area. Important regional features include the Wallowa Bullseye (WB), the Wallowa Range (WR), the Enterprise Moat (EM), the Blue Mountain Range (BMR), the Blue Mountain Province (BMP), the Western Snake River Plane (WSRP), the Idaho Batholith (IB), and the Central Columbia Basin (CCB). Of particular note, a distinction is made between the Blue Mountain Range (BMR), and the Blue Mountain Province (BMP). Here we propose a tectonophysical interpretation of the structures surrounding the Wallowa Mountains, in which large sills transported mid-crustal melt from the WSRP into the BMP during the Miocene. We suggest that these basaltic intrusions thickened the BMP's crust, producing a broad plateau. Subsequent foundering of the Wallowa Batholith's dense eclogite root entrained nearby crust, forming a concentric "moat" that separates the modern Wallowa Range from the rest of the BMP. The resulting structures form a striking bullseye-like topographic expression, centered on the Wallowa Range.

3.3.2 Columbia River Flood Basalts

Columbia River Flood Basalt erupted across much of eastern Oregon, climaxing in the middle Miocene with the Grande Ronde event. Grande Ronde flows erupted from the Chief Joseph Dike Swarm, whose exposure is centered within the Wallowa bullseye (Taubeneck, 1970). The Grande Ronde unit represents over 70% of the total CRB group by volume, and erupted in as little as 100 ky (Kasbohm & Schoene, 2018; Reidel et al., 2013). Although the CRB's are commonly attributed to arrival of the Yellowstone plume in continental North America, several key details of their existence are yet to be reconciled with this basic interpretation.

Most strikingly, the eruptive centers propagated northward, with the largest eruptions sourced from fissures hundreds of kilometers away from the projected location of Yellowstone (Reidel et al., 2013). Based on upper mantle seismic images that resolve what appears to be a hanging fragment of Farallon slab, we interpret that this shift was caused by propagating slab removal, triggered by arrival of the Yellowstone plume (Darold & Humphreys, 2013; Hales, Abt, Humphreys, & Roering, 2005).

Other prominent interpretations for this observation include: a trench-parallel tear in the Juan de Fuca slab, enabling hot sub-slab mantle to ascend and decompress through an elongate window (Liu & Stegman, 2012); or decompression melting of the Yellowstone plume head as it flowed "uphill" from thick continental lithosphere, toward the thin lithosphere of the accreted terrains (Camp & Hanan, 2008; Thompson & Gibson, 1991). While seismic images support our preferred slab-removal hypothesis, they do not preclude either of these interpretations.

Based on a range of geochemical analyses, Wolff, Ramos, Hart, Patterson, and Brandon (2008) showed that CRB's were likely sourced from a deep mantle

plume, but most units exhibit mineralogical and chemical evidence of assimilation with Precambrian North American crust. We follow their interpretation that Yellowstone heat helped built a large, centralized melt reservoir around the location of the modern WSRP. There is, however, significant heterogeneity between CRB units, suggesting the existence of multiple magma reservoirs with diverse histories.

3.3.3 Structural Deformation

At the time of GR eruptions, the Wallowa Batholith appears to have occupied the center of a broad regional uplift, which we refer to as the "Chief Joseph Plateau." Observations of structural deformation, fluvial geomorphology, and catchment organization, all support this interpretation.

Structurally, CRB flows fold anticlinally over the Blue Mountains, connecting the Columbia Basin to the Enterprise Moat (Burns, Morgan, Peavler, & Kahle, 2011; Hales et al., 2005). Continuous flows across the peripheral bulge require that the moat sat equal to, or higher than the Blue Mountains at the time of Grande Ronde eruptions. CRB lava, including Grande Ronde flows, deposited primarily to the north, implying a regional slope towards a deepening Columbia Basin (Perry-Houts & Humphreys, 2018).

While likely high during the Miocene, the Chief Joseph Plateau was at lower elevation than the Idaho Batholith. Sub-CRB gravel deposits atop the Wallowas indicate that parts of central Idaho drained across the area prior to CRB deposition (Allen, 1991). This observation implies that the WB was not a significant topographic feature, an interpretation also supported by the unusual drainage pattern within the Wallowas.

Throughout the Wallowas, many valleys take routes that appear unfavorable based on modern topography. The Minam River, for example, one of the largest

river valleys in the Wallowas, runs north-northwest, parallel with the range's long axis. One would expect erosional processes to favor a direct path toward lower elevation, but the Minam takes nearly the *longest* straight-line path from the central range to the moat, suggesting that it follows a paleodrainage that predates the recent uplift.

The moat, too, appears to be a recent feature that Miocene rivers did not see. Organization of post-CRB catchments supports the interpretation that area was part of a broader highland, with no clear internal topographic prominence. Carson and Spencer (1995) found deposits on the south slope of the BMR that Trout Creek recently reversed its flow direction. Trout Creek now flows south, through a well-developed river valley that straddles the Blue Mountains. The modern drainage divide between Trout Creek and Joseph Creek is part of a continuous, deep valley that connects the two streams, suggesting that the Enterprise area drained directly north as recently as the late Pliocene. Adjacent valleys form similar structures, further supporting the interpretation that the Enterprise area once drained directly to the north, over a continuous slope from the Wallowas to Lewiston.

3.4 Interpretation

So far, we have shown evidence that, in combination, suggests a cohesive narrative for evolution of the Wallowa bullseye. In summary, prior to the Miocene, the Blue Mountain Province was mostly flat, and sat downstream of the central Idaho Batholith. The whole BMP appears to have uplifted into a broad plateau, coeval with CRB eruptions. Finally, the moat subsided into the young plateau, forming the coaxial bullseye pattern.

The form of these epeirogenies suggests that they were not generated by horizontal tectonic stresses. Rather, each phase seems to be associated with a change in density structure that adjusted the isostatic balance of the local crust.

First, subsidence of the moat seems to have been driven by direct vertical stresses. While some faults in the moat's southwest quadrant can be plausibly attributed to regional tectonic extension, the Wallowa Fault, on the northeast flank of the WR, tells another story.

Most normal faults are associated with a down-flexed hanging wall, against an up-tilted foot wall, as predicted for an isostatically-supported extending plate. In contrast, the Wallowa Fault's hanging wall bends upward, forming the Alder Slope, a broad, gentle incline between Enterprise and the Wallowa range (Carson & Spencer, 1995). We interpret this 'abnormal' fault as evidence that moat subsidence is driven not by horizontal tectonic stresses, but by dynamic changes in isostatic load.

In combination with the common interpretation that Wallowa uplift resulted from removal of dense mafic cumulate, we take the dynamic subsidence of the moat as indication that adjacent crust was entrained with the foundering root. This closely aligns with the results of H. Wang and Currie (2017), who found that root foundering can thin the nearby crust, as ductile layers are entrained by Poisselle flow. Further, we suggest that the radial symmetry of the Wallowa bullseye system will exaggerate this effect close to the foundering root.

The Chief Joseph Plateau, however, remains enigmatic. We propose that it developed as a response to mid-crustal magma transport, as incipient delamination and foundering applied vertical traction to the lower crust of the BMP. The complete tectonic setting we envision for the Miocene Wallowa area is illustrated in

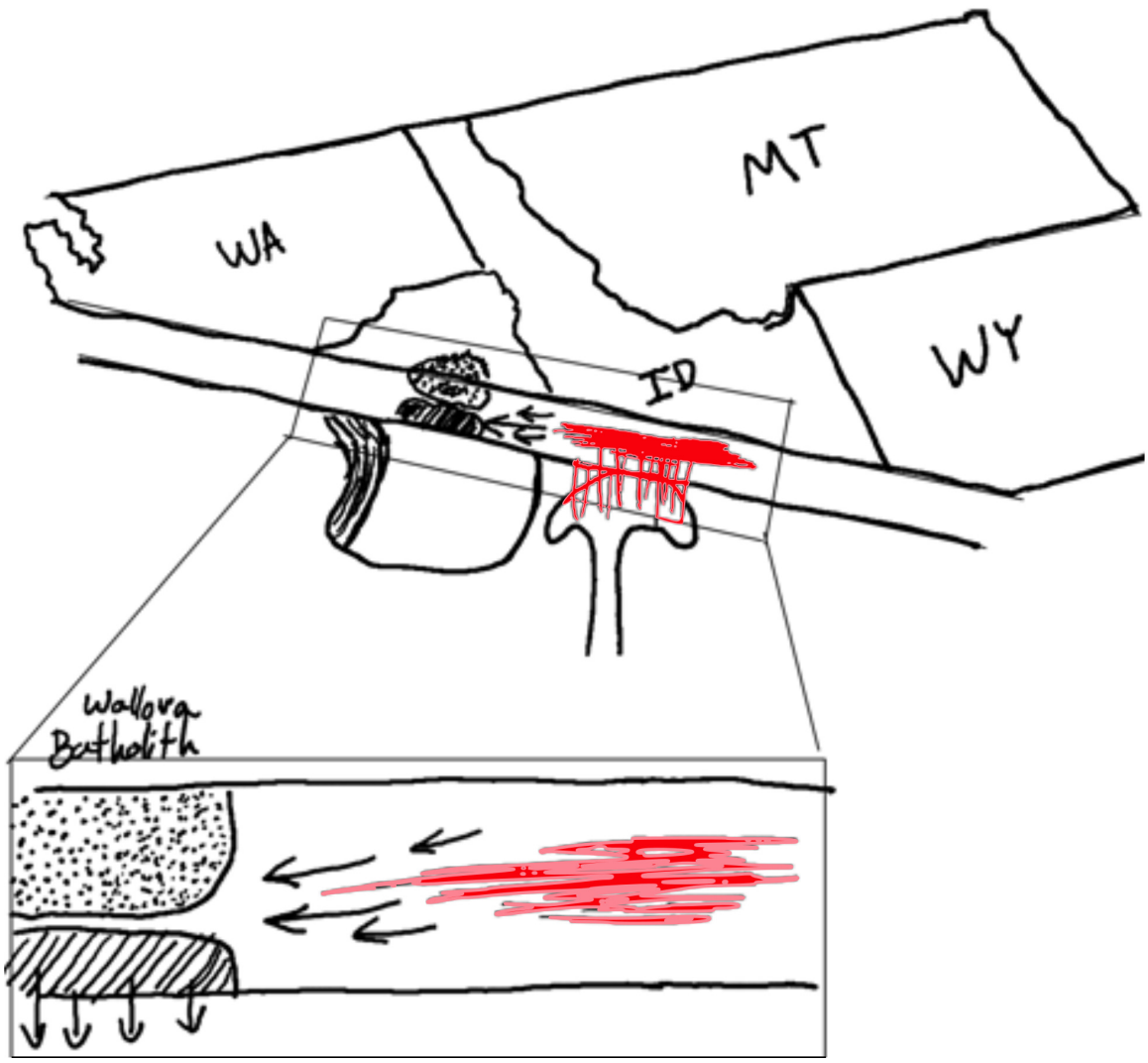

Figure 3.2. The weight of both delaminating Farallon slab, and the Wallowa Batholith's dense root, created localized vertical extension that directed sills from the Western Snake River Plane towards the Blue Mountains.

Figure 3.2. Schematically, the sequence of events leading to the modern topography are shown in Figure 3.3.

3.5 Models

Our geophysical interpretation of the Wallowa bullseye requires that density anomalies in the lower crust and upper mantle are able to control propagation of mid-crustal magmatic intrusions, by applying localized vertical traction. To test this idea, we have developed numerical models of heterogeneous crust in the presence of a proximal melt reservoir. Preliminary models indicate that the load of an eclogitic root can affect sill propagation, suggesting that deep structures can efficiently direct magmatic intrusions within the crust.

3.5.1 Equations

We aim to simulate melt transport within the crust through open fissures. However, because the continuum formulation of fracture mechanics introduces complicating nonlinearities (Bangerth, Dannberg, Gassmöller, Heister, & others, 2017), we simulate melt transport as percolation through a ductile, compressible, and permeable host rock (e.g. McKenzie, 1984).

We use the mathematical formulation of Keller, May, and Kaus (2013) in the viscous limit, extended for compressible solid and fluid phases, as implemented in ASPECT `ver 2.0.1` (Bangerth et al., 2017; Dannberg & Heister, 2016; Kronbichler, Heister, & Bangerth, 2012). This choice has the effect of smoothing melt migration, as it does not promote melt channelization. The forces driving melt transport, and the melt's effect on viscous flow in the host rock, are identical in either case.

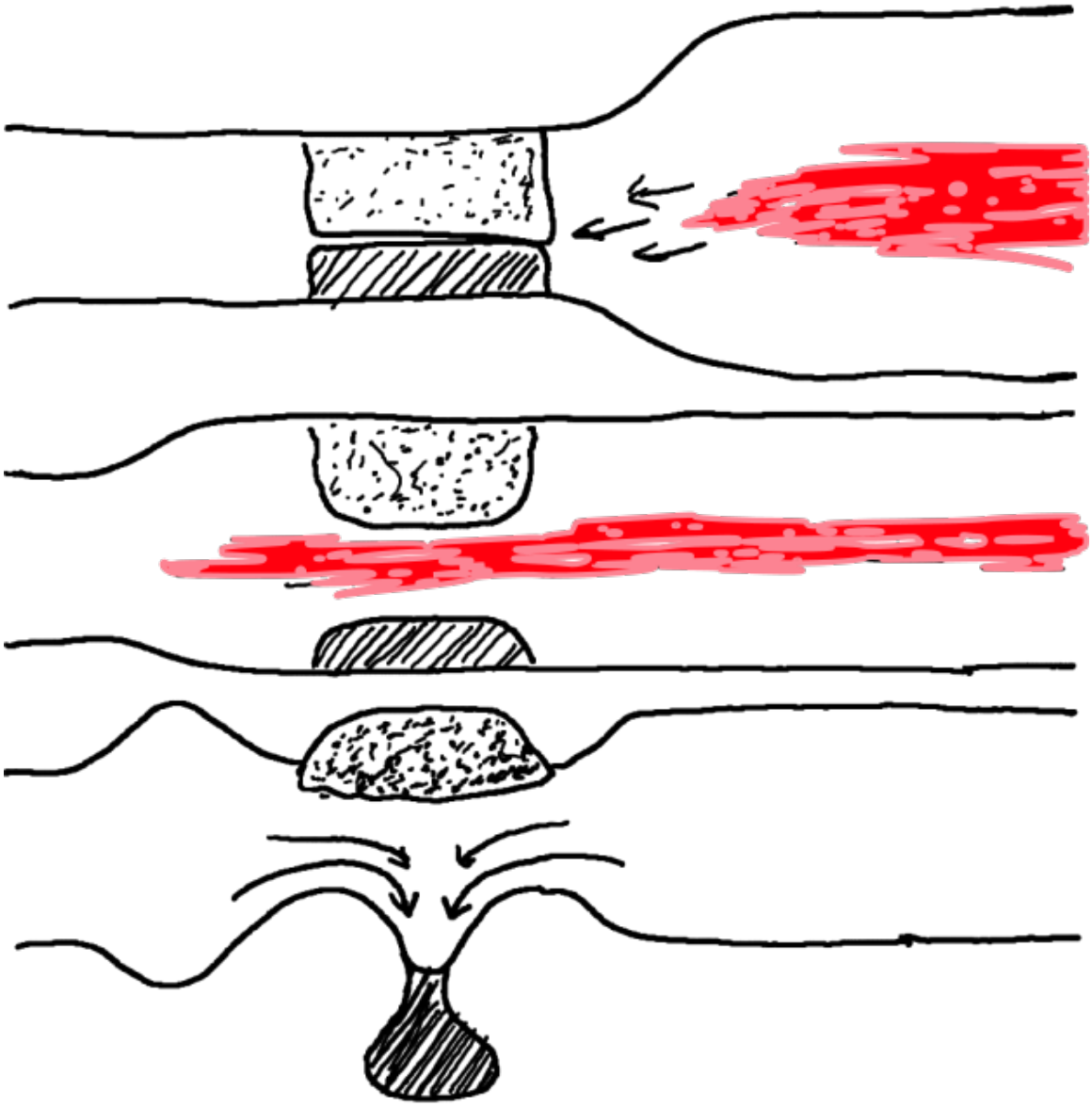

Figure 3.3. Lateral pressure gradients between the Blue Mountain Province and continental Snake River Plane promoted sill propagation and crustal inflation throughout the Wallowa area, mechanically separating the batholith's eclogite root. Subsequent foundering of the dense root evacuated crust around the pluton, creating a circumferential moat.

3.5.2 Model Setup

Our model domain is a 2D-Cartesian rectangle, with spatial dimensions 600×150 km. We track changes in topography with passive tracer particles, embedded in the ductile flow field, below an upper layer of "sticky air."

Host rock flow velocity, $\mathbf{u}$, is constrained at the model boundaries. The bottom boundary is no-slip ($\mathbf{u}_x = 0$), and the upper boundary is stress-free ($\nabla \mathbf{u} = 0$). We impose a moderate $1\,\mathrm{cm\,yr^{-1}}$ outward flow to both side boundaries (for a total $2\,\mathrm{cm\,yr^{-1}}$ extension) in the upper 100 km, to approximate the tectonic environment of the Miocene BMP.

Initial model geometry, and material parameters, are listed in table 3.1. The initial conditions are meant to simulate a density-stratified batholith adjacent to a buoyantly stable mid-crustal melt reservoir. We do not currently simulate thermodynamic evolution of the melt, including phase changes and associated latent heat release or absorption. Melt does advect heat through the host rock, significantly modifying the crust's thermal structure over time (e.g. Karlstrom, Paterson, & Jellinek, 2017).

3.5.3 Model results

Preliminary models demonstrate the ability of deep density anomalies to guide sill emplacement, as shown in Figure 3.4. In addition to building a crustal welt, the sills will mechanically detach a pluton's dense root, accelerating its foundering. This supports the concept, proposed by Perry-Houts and Karlstrom (2018), that igneous intrusions can destabilize the lithosphere, promoting crustal or lithospheric delamination.

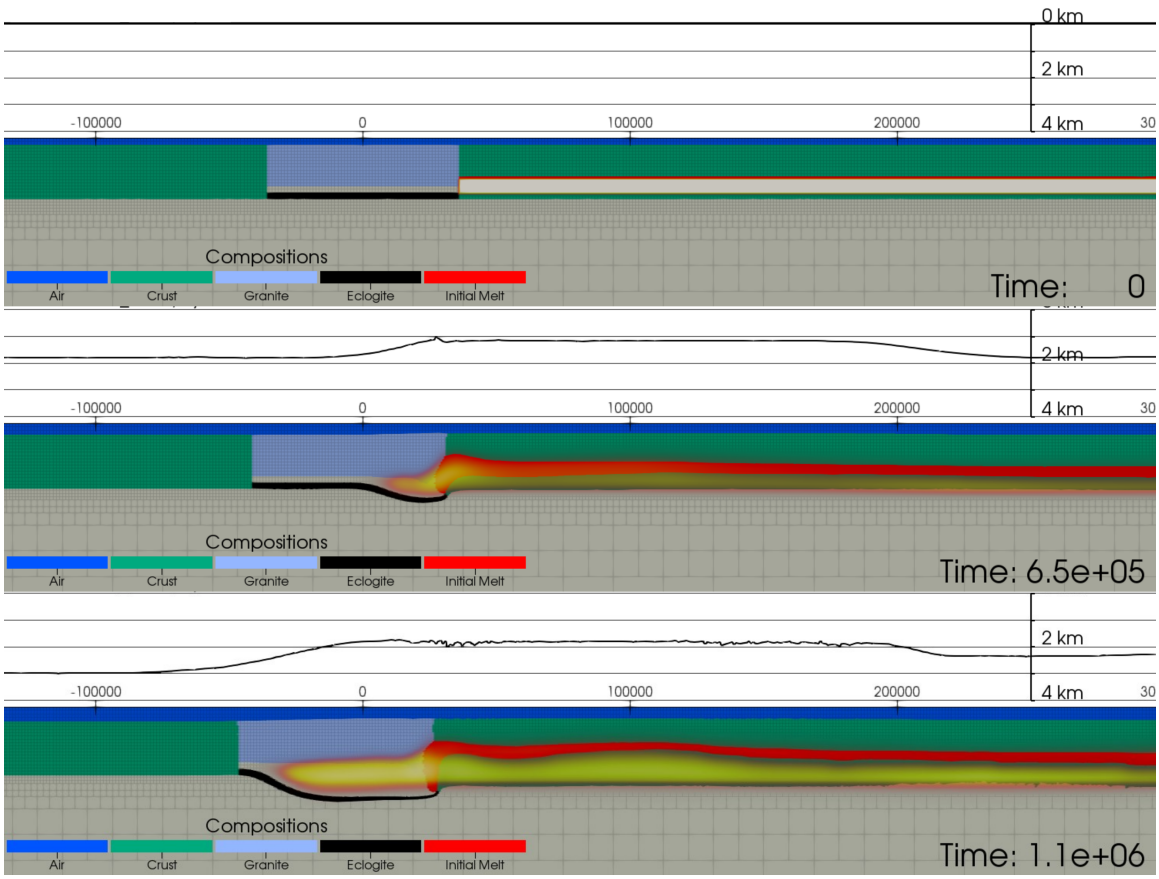

Figure 3.4. Zoomed snapshots of preliminary sill-propagation models. By allowing melt to propagate independently of the deforming host rock, we see a clear tendency for dynamically low-pressure mid crust to drive lateral flow of nearby melt bodies. As the fluid surface sinks through time, owing to imposed boundary extension, crustal inflation by magma transport raises topography around the stratified batholith, creating a localized plateau. Melt is represented in the red-yellow color map, overlain on the more schematically represented host rock lithologies. Model properties, including the Newtonian viscosities of each lithologic domain, are listed in Table 3.1.

Parameter	Symbol	Value	Units
Mantle density	ρ_m	3300	$\mathtt{kg.m^{-3}}$
Crust density	ρ_c	2900	$\mathtt{kg.m^{-3}}$
Melt density	ρ_ϕ	2900	$\mathtt{kg.m^{-3}}$
Basalt density	ρ_b	2800	$\mathtt{kg.m^{-3}}$
Eclogite density	ρ_e	3550	$\mathtt{kg.m^{-3}}$
Mantle viscosity	η_m	1×10^{22}	$\mathtt{Pa.s}$
Crust viscosity	η_c	1×10^{28}	$\mathtt{Pa.s}$
Melt viscosity	η_ϕ	1×10^{18}	$\mathtt{Pa.s}$
Granite viscosity	η_b	1×10^{23}	$\mathtt{Pa.s}$
Eclogite viscosity	η_e	1×10^{22}	$\mathtt{Pa.s}$
Thermal conductivity	k	4.7	$\mathtt{W.m^{-1}.K^{-1}}$
Thermal bulk viscosity exponent	β	7	None
Reference bulk viscosity	ξ_0	1×10^{19}	$\mathtt{Pa.s}$
Reference permeability	k_ϕ	1×10^{-8}	$\mathtt{m^2}$
Solid compressibility	κ_s	4.2×10^{-12}	$\mathtt{Pa^{-1}}$
Melt compressibility	κ_m	1.25×10^{-11}	$\mathtt{Pa^{-1}}$

Table 3.1. Parameters for sill propagation modeling.

3.6 Discussion

The events proposed here are unique to the recent tectonic history of northeast Oregon. However, the processes are much more general. While many of the primary interpretations have previously been discussed regarding the Wallowas (Darold & Humphreys, 2013; Elkins-Tanton, 2007; Farmer et al., 2008; Göğüş & Pysklywec, 2008; Hales et al., 2005; Saleeby, Ducea, & Clemens-Knott, 2003; H. Wang & Currie, 2017), we have additionally proposed a novel mechanism for crustal melt transport that we believe deserves some attention.

Many studies on melt transport focus on the density and strength of overlying and nearby crust. Often, features such as topography are considered as primary driving forces for crustal magma transport. Our findings suggest that deep structures can generate significant stress in the crust, and should not be neglected when investigating melt transport dynamics. Our preliminary models do, however,

omit many important physical mechanisms that we expect will have low-order effects on their results.

As discussed in Section 3.5.1, we consider melt transport as porous flow through a compressible host rock. In reality, melt transport in the crust often creates or exploits existing brittle fractures, through which it may flow relatively unimpeded. This channelization effect can be modeled with a continuum formulation (e.g. Keller et al., 2013), but we have yet to implement the full viscoelastic-plastic rheology necessary for such a model. While melt transport responds to the same dynamic pressure gradients with or without nonlinear host rock deformation, we expect that the channelization effect will play an important role in determining the geometry and rate of melt transport.

Additionally, we do not yet consider the thermodynamic effects of melting and freezing. Melt in our model is constrained to a predetermined volume, initialized as a wide regional magma reservoir in the mid-crust. We expect the inclusion of melting, freezing, and associated latent heat accounting to have a major effect on the magnitude and timescales of all modeled processes. In fact, we rely on sill freezing to generate a crustal viscosity profile conducive to the moat-forming processes of H. Wang and Currie (2017).

We hope to implement both of these features in the near future. Their inclusion will help constrain the length and timescales in which our tectonophysical interpretation can be considered plausible. For now, we are confident that the dynamic stress generated by deep structures can be strong enough to affect crustal magma transport. But we cannot yet quantify much about the physical scales required to fit our tectonic interpretation of the Wallowa bullseye.

3.7 Conclusion

Here we have proposed sequence of events that we believe led to formation of the Wallowa bullseye. Much of our interpretation follows the work of others, which we have combined into a single, cohesive narrative. Further, we have suggested the possibility that deep density anomalies can guide magmatic intrusions, by creating lateral pressure gradients in the crust.

Geodynamic models support our interpretation, suggesting that deep (lower crust and upper mantle) density structure can affect shallow melt transport. Our models are still in a preliminary state, however, and further testing will be required to validate our findings. So far, we can infer with some confidence that deep structures are capable of generating non-negligable dynamic pressure within the lithosphere. We suggest that these mechanisms should not be overlooked when modeling crustal melt dynamics.

3.8 Bridge

The story proposed here is specific to the Miocene Pacific Northwest. It remains to be seen whether these phenomena exist elsewhere in the world, and especially in association with other large igneous provinces. In particular, we have drawn a connection between igneous intrusions and lithospheric delamination, which deserves further investigation. In the following chapter, we will explore the generalized geodynamic consequences of igneous intrusions, and whether their presence can promote destabilization of lower crust and mantle lithosphere.

CHAPTER IV

ANISOTROPIC VISCOSITY AND TIME-EVOLVING LITHOSPHERIC INSTABILITIES DUE TO ALIGNED IGNEOUS INTRUSIONS

From Perry-Houts, J., & Karlstrom, L. (2018). Anisotropic viscosity and time-evolving lithospheric instabilities due to aligned igneous intrusions. *Geophysical Journal International*. doi: https://doi.org/10.1093/gji/ggy466. The ideas presented in this chapter came from many discussions with Leif Karlstrom, and others. Leif provided lots of scientific insight, and content edits. I developed and implemented the models and analyses, and wrote all the text.

4.1 Summary

Anisotropic viscosity is often discussed in the context of flow-induced crystallographic alignment, also known as lattice-preferred orientation, believed to exist throughout the mantle. However, other geophysical systems can produce bulk anisotropic rheology. One example is so-called shape-preferred orientation, such as that imparted by repeated, non-randomly oriented igneous intrusions. Dikes and sills tend to intrude perpendicular to least compressive tectonic stress, and therefore are typically aligned with other coeval intrusions. Intrusions provide distinct planes of weakness, producing, in a bulk sense, an anisotropic fabric to the rocks in which they are intruded. We parameterize this style of anisotropic viscosity with an effective-medium approximation, based on analytically derived characteristics of layered media. We find that the magnitude of anisotropy is highly sensitive to the presence of weak layers, even if they are relatively thin and/or sparsely distributed. We test the effects of our constitutive law on Rayleigh-Taylor instability growth, representing lithospheric instabilities. Our results indicate dramatically decreased stability of lithosphere intruded by dikes and/or sills.

4.2 Introduction

Viscous flow is the dominant mechanism of deformation in the bulk Earth. Mechanisms that govern rheology are thus of great concern to the Earth sciences. Much work has been done to understand and quantify these mechanisms for polycrystalline rocks (e.g. Hirth & Kohlstedt, 2003).

Interest has grown in understanding the presence of anisotropy in rock physics. Most work on the subject focuses on anisotropy resulting from strain-induced crystal-lattice-preferred orientation (LPO) in olivine (Hansen, Warren, Zimmerman, & Kohlstedt, 2016; Tommasi et al., 2009; Wendt, Mainprice, Rutter, & Wirth, 1998) and on its relevance to mantle flow dynamics (U. R. Christensen, 1987; Richter & Daly, 1978; Saito & Abe, 1984), lithospheric deformation of oceanic shear zones (Michibayashi & Mainprice, 2004), and continental rifting (Vauchez, Tommasi, & Barruol, 1998).

Anisotropy also manifests on larger scales, such as that due to brittle cracks, sedimentary layering, and shear-induced melt segregation (Crampin, 1978; Holtzman et al., 2003; Moore, Garnero, Lay, & Williams, 2004; Mühlhaus, Moresi, Hobbs, & Dufour, 2002). These types of mechanisms are collectively referred to as shape-preferred orientation (SPO).

Magmatic intrusions are an example of SPO which have received little attention. Intrusions tend to form perpendicular to the orientation of the least compressive stress. Therefore, coeval, proximal dikes tend to be preferentially aligned with one another. Such systems manifest on a variety of length-scales, from individual volcanic edifices to continent-scale swarms (Hou, 2012).

The disparate length-scales inherently involved in these systems make modeling their dynamics difficult. Generic mechanical models exist to describe layered media (e.g. Mühlhaus et al., 2002), but no framework exists to predict

anisotropic material properties in these systems. We develop an effective-medium approximation for SPO properties resulting from aligned igneous intrusions that enables the inclusion of this form of viscous anisotropy in geodynamic models.

Lithosphere may be gravitationally unstable relative to underlying mantle, owing to a combination of thermal, compositional, and tectonic effects (Houseman, McKenzie, & Molnar, 1981; Kay & Kay, 1993). Its viscosity is therefore important in establishing long-term stability. Density-driven lithosphere removal can take many forms, but is commonly approximated by Rayleigh-Taylor instabilities (Beall, Moresi, & Stern, 2017; Conrad & Molnar, 1997). Previous studies of anisotropic Rayleigh-Taylor instabilities primarily investigated analytic linear stability models, without significant analysis of time-dependence, and with intended application to lithospheric LPO (Lev & Hager, 2008).

We implement our proposed rheology in the community finite element software, ASPECT (Gassmöller, Heien, Puckett, & Bangerth, 2016; Heister, Dannberg, Gassmöller, & Bangerth, 2017; Kronbichler et al., 2012), to test its effect on long-term lithosphere dynamics. We investigate time-evolving Rayleigh-Taylor instabilities of lithosphere with a range of anisotropic parameters, representing intrusive volcanic systems. Our models demonstrate the significance of igneous intrusions on lithosphere stability, as well as the importance of time-dependence in modeling lithosphere dynamics.

4.3 Governing equations

We consider deformations for which momentum balance is well-approximated by low-Reynolds number, gravity-driven flow,

$$\tau_{ij,j} - p\delta_{ij} + \rho g_i = 0, \tag{4.1}$$

with deviatoric stress, τ_{ij}; density, ρ; gravity, g_i; pressure, p; and the Kronecker delta, δ_{ij}. Commas in subscripts denote spatial derivatives with respect to the following index. Flow must also satisfy the mass-balance continuity equation

$$(\rho u_i)_{,i} = 0 \tag{4.2}$$

where u_i is velocity.

Additionally, we track compositional fields which advect with velocity u_i,

$$\dot{c}_x + u_i c_{x,i} = q_x, \tag{4.3}$$

with a distinct source term, q_x, for each field, c_x, and overdot representing a derivative with respect to time.

Linear rheology is described by a fourth-order constitutive tensor, C_{ijkl}, which maps strain rate to deviatoric stress without loss of generality,

$$\tau_{ij} = 2C_{ijkl}\dot{\varepsilon}_{kl}, \tag{4.4}$$

where $\dot{\varepsilon}_{ij} = \frac{1}{2}[u_{i,j} + u_{j,i}]$ is the strain rate.

One of the simplest forms of anisotropy is called transverse isotropy (TI), defined by a single anomalous plane (Honda, 1986; Mühlhaus et al., 2002; Saito & Abe, 1984). Building on Saito and Abe (1984), Honda (1986) showed that a TI rheology may be parameterized by two scalars– a normal viscosity (η_N), and a shear viscosity (η_S), activated in pure shear, and simple shear with respect to the orientation of the material fabric, respectively. This constitutive behavior implicitly depends on the orientation of anisotropy, which we denote using a vector, n_i, normal to the material fabric. Pure and simple shear are defined relative to n_i such that

$$\dot{\varepsilon}_{ij}n_i = \begin{cases} \dot{\varepsilon}_{11}n_1 + \dot{\varepsilon}_{22}n_2 & \text{in pure shear,} \\ \dot{\varepsilon}_{21}n_1 + \dot{\varepsilon}_{12}n_2 & \text{in simple shear.} \end{cases} \tag{4.5}$$

Following Mühlhaus et al. (2002), we employ a TI constitutive law that modifies the standard viscosity along a single plane,

$$\tau_{ij} = 2\eta_N \dot{\varepsilon}_{ij} - 2(\eta_N - \eta_S)\Lambda_{ijkl}\dot{\varepsilon}_{kl}, \tag{4.6}$$

where Λ is a fourth-order tensor that imparts orientation-dependence, relative to n_i,

$$\Lambda_{ijkl} = \frac{1}{2}(n_i n_k \delta_{lj} + n_j n_k \delta_{il} + n_i n_l \delta_{kj} + n_j n_l \delta_{ik}) \\ -2n_i n_j n_k n_l. \tag{4.7}$$

The director orientation, n_i, varies in time as a function of the deformation gradient,

$$\dot{n}_i = \left[u_{i,j} - \dot{\varepsilon}_{ij} - \dot{\varepsilon}_{ki} n_k n_j + \dot{\varepsilon}_{kj} n_k n_i\right] n_j. \tag{4.8}$$

Because energy is not dissipated under solid-body rotation, the constitutive equation (4.6) deals only with the symmetric part of the velocity gradient. As a result, C_{ijkl} must also be symmetric. For a fourth-order tensor that means $C_{ijkl} = C_{jikl} = C_{ijlk} = C_{jilk}$. Therefore, the material model is insensitive to differences between orthogonal senses of the same simple shear.

Entropy also requires that C_{ijkl} be positive definite, that is, the material must dissipate a positive amount of energy under any deformation. Therefore, the full constitutive law must also be insensitive to differences between pure shear which is normal or parallel to n_i. Thus, we make no distinction between materials with orthogonal planes of anisotropy. The most distinct fabric orientations are then oriented 45° relative to one another (i.e. $n_i^A n_i^B = \sqrt{2}/2$, for materials, A, and B). In the following sections we compare models with horizontal, and 45° dipping fabrics, following the approach of Lev and Hager (2008).

4.4 Effective-medium approximation

In order to prescribe values for η_N and η_S, we need to understand the bulk effect of material layering. Kendall and Silver (1998) define an effective-medium for TI seismic anisotropy, based on the model of Tandon and Weng (1984) that assumes oblate inclusions of distinct material properties. Because dikes and sills are large, continuous features, they more closely approximate the limiting case of large-aspect-ratio inclusions, or laminate layering (Backus, 1962). This assumption allows us to solve analytically for exact values of shear and normal viscosity as functions of individual layer properties.

We begin by defining a representative volume element (RVE) which spans a typical, 'statistically homogeneous,' volume of the real material (R. M. Christensen, 2005). For the case of igneous intrusions, the natural RVE is a column of rock whose height, h, encompasses a cycle from one intrusion to the next; i.e. a layered stack which contains a dike or sill, and a layer of host rock (Fig. 4.1A). We assume that layer-parallel deformation is uniform, which reduces our RVE to a 1-dimensional profile of length h. We retain the volume element terminology for consistency with other work.

In defining an effective-medium, we aim to find a homogeneous fluid that behaves comparably over h as the RVE does (Hashin, 1983). We formulate our homogenization in terms of power flux,

$$\int_0^h \eta^e \dot{\varepsilon}^e_{ij} \dot{\varepsilon}^e_{ij} dz = \int_0^h \eta \dot{\varepsilon}_{ij} \dot{\varepsilon}_{ij} dz, \tag{4.9}$$

with RVE viscosity, η; effective viscosity, η^e; and strain rate fields within the RVE and effective models, $\dot{\varepsilon}$, and $\dot{\varepsilon}^e$, respectively.

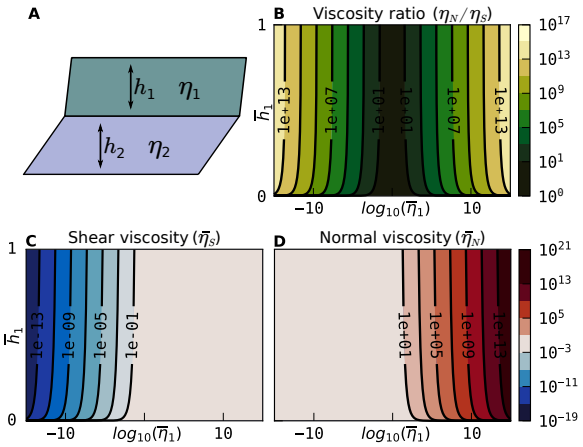

Figure 4.1. Effective viscosity of a periodic, two-layer medium as a function of layer viscosity and thickness ratios. Axes are shared between sub-figures **B-D**. Variables with overbars are normalized to the equivalent property in layer 2. **A**: Schematic representation of a layered medium, representing a dike-host rock cycle. **B**: Ratio of shear to normal viscosity, demonstrating that anisotropy magnitude is highly sensitive to the viscosity ratio, and insensitive to relative thickness of the layers. **C-D**: Shear viscosity and normal viscosity on same axes as **B**, demonstrating that simple-shear deformation is primarily sensitive to properties of the weaker layer, while normal viscosity is more sensitive to the stronger layer.

4.4.1 Normal viscosity

Under pure shear, strain rate within the RVE is uniform, and equation (4.9) reduces to

$$h\eta_N^e = \int_0^h \eta(z)dz, \tag{4.10}$$

for effective normal viscosity, η_N^e.

In the discretized, N-layer case, equation (4.10) can be written as the weighted arithmetic mean of the RVE constituent viscosities,

$$\eta_N^e = \frac{\Sigma_{i=1}^N \eta_i h_i}{\Sigma_{i=1}^N h_i}, \tag{4.11}$$

where η_i and h_i are viscosity and thickness of layer i, respectively.

4.4.2 Shear viscosity

In simple shear, the strain rate field within the same RVE is non-uniform because weak layers can accommodate more strain than strong layers.

To find a homogeneous effective shear viscosity, we first simplify equation (4.9) by noting that strain rate must be continuous. Therefore, stress must be constant throughout both the RVE and effective column, reducing equation (4.9) to

$$\int_0^h \tau_{ij}\dot{\varepsilon}_{ij}^e dz = \int_0^h \tau_{ij}\dot{\varepsilon}_{ij} dz. \tag{4.12}$$

By inverting the linear, isotropic constitutive law of the individual layers, we get

$$\dot{\varepsilon}_{ij} = \frac{\tau_{ij}}{\eta}, \tag{4.13}$$

and equation (4.12) further reduces to

$$\frac{h}{\eta^e} = \int_0^h \frac{1}{\eta} dz. \tag{4.14}$$

Similar to our derivation of equation (4.11), for the case of a discretized medium, equation (4.14) can be written

$$\eta_S^e = \frac{\Sigma_{i=1}^N h_i}{\Sigma_{i=1}^N \frac{h_i}{\eta_i}}. \tag{4.15}$$

That is, the weighted harmonic mean of the RVE's constituent viscosities.

Equation (4.15) shows that shear viscosity is highly sensitive to the viscosity of the weakest layer, and insensitive to the relative layer thicknesses, suggesting that, for example, a sparse distribution of molten sills can reduce the effective shear viscosity of its host to near that of liquid magma (Fig. 4.1). In comparison, equation (4.11) is highly sensitive to the presence of strong layers, and insensitive to the properties of weak layers. Therefore, a weak host rock dissected by solidified sills, for example, may become substantially stronger under normal shear than it

was without the intrusions. The difference between the two viscosities defines the system's magnitude of anisotropy, and suggests that SPO can have profound effects. Here we define anisotropy magnitude as $1 - \eta_S/\eta_N$, such that the magnitude is zero for isotropic materials, and asymptotically approaches 1 as the ratio of shear to normal viscosity decreases.

For example, the Mesoproterozoic Mackenzie igneous events occurred within a short duration, erupting over $650,000$ km^3 of basalt through a 2400 km $\times$ 1800 km dike swarm exposed in the northern Canadian Shield (Gittings, 2008). The region averages one 30 meter thick dike per 72 kilometers across strike (LeCheminant & Heaman, 1989). Assuming an average dike viscosity of approximately 10^3 Pa $\cdot$ s during emplacement, and an average host viscosity approximately 10^{23} Pa $\cdot$ s, we expect an effective shear viscosity, $\eta_S^e \approx 2.5 \times 10^6$ Pa $\cdot$ s, and normal viscosity, $\eta_N^e \approx 9.9 \times 10^{22}$ Pa$\cdot$s. This represents a shear viscosity reduction of almost 17 orders of magnitude, substantially higher than that from olivine LPO, which produces approximately one order of magnitude in shear viscosity reduction (Hansen et al., 2016; Hansen, Zimmerman, & Kohlstedt, 2012).

4.4.3 Limitations

We make several significant assumptions in this effective medium formulation that deserve further discussion.

First, we assume that magmatic intrusions have infinite planar extent. This assumption holds so long as anisotropic model cells have at least one continuous through-going intrusion, and discontinuous intrusions are separated by a resolvable distance. It does not hold for intrusions smaller than discretization scale, or rocks with very widely spaced intrusions where the composite cannot be considered statistically homogeneous.

Second, we assume that buckling instabilities do not develop with wavelengths smaller than discretization. In such a case, layer-parallel simple shear along the weak layers will begin to accommodate strain under macroscopic pure shear (Schmalholz & Podladchikov, 2001). This scenario violates the assumption in Section 4.4.1 that strain rate is uniform under pure shear. Effective normal viscosity in this case will decrease, reducing the net magnitude of anisotropy.

Systems for which our assumptions do not hold may still exhibit viscous anisotropy, and therefore may be analyzed in the context of our parameter space search (Sec. 4.5.2; Fig. 4.2), but the effective medium developed here does not directly apply. We argue that our model is a good fit for large dike swarms, such as those emplaced during flood basalt eruptions, where dikes can be hundreds of kilometers long, and tens of meters thick.

4.5 Geodynamic models

We have shown that the presence of mechanically distinct layers, such as those produced by igneous intrusions, significantly modifies the bulk rheology of the host rock (Sec. 4.4; Fig. 4.1). Following Lev and Hager (2008), we hypothesize that this will affect lithospheric instabilities in volcanically-active regions.

To test our hypothesis, we solve equations (4.1)–(4.8), (4.11), and (4.15) with ASPECT version `2.0.0-pre` (Bangerth et al., 2017). We run a Monte Carlo ensemble of unstably-stratified models with various anisotropic and geometric parameters to analyze the effect of viscous anisotropy on long-term growth properties of Rayleigh-Taylor instabilities. All code and documentation required to reproduce these results can be found in the supplemental files included with this dissertation.

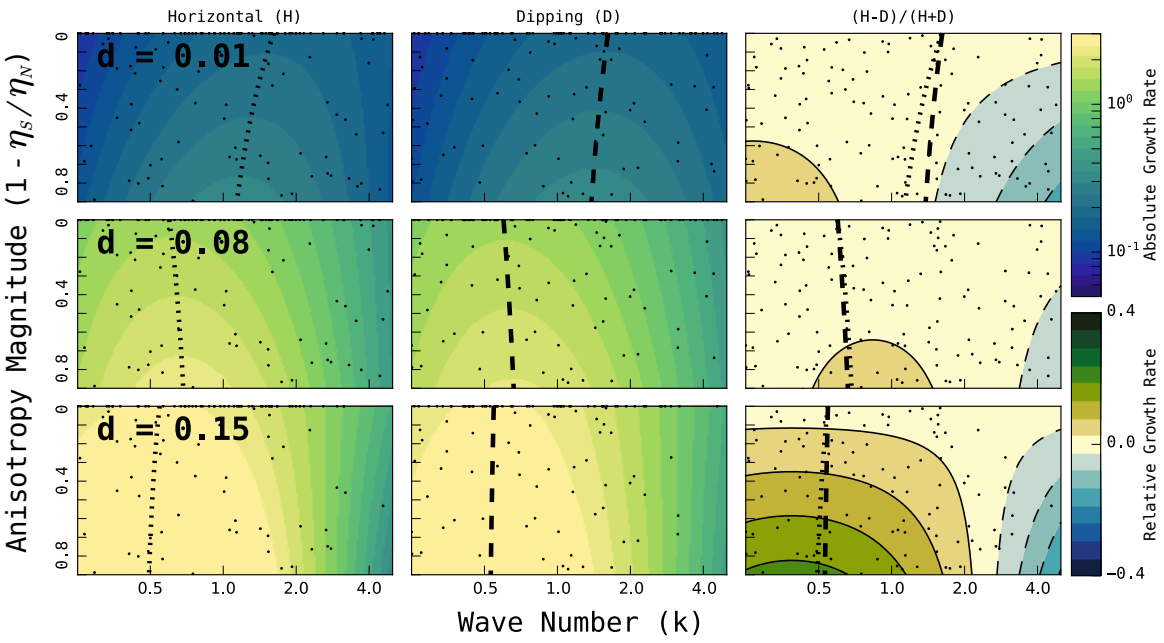

Figure 4.2. Snapshots of instability growth rate through model time. We sample instability growth rates from an ensemble of anisotropic Rayleigh-Taylor models (black dots) when each one reaches specified fluid interface displacement distances, $\mathbf{d} = \{0.01, 0.08, 0.15\}$ (subplot rows). Each model has an anisotropic, dense, upper layer, with either horizontal (H), or dipping (D) initial fabric (Fig. 4.3), fixed anisotropy magnitude, $1 - \eta_S/\eta_N$, and fixed wavenumber, k. We fit a parabolic surface to the ensemble's modeled growth rate in each snapshot, as a function of wavenumber and anisotropy magnitude. Best fit surfaces for the horizontal models and dipping models are shown in the left, and middle columns, respectively, with warmer colors representing faster instability growth. The normalized difference between horizontal and dipping models is plotted in the right column, where areas of parameter space where horizontally anisotropic models outpace dipping models are shown in green, and vice versa in blue. The most unstable wavenumber, as a function of anisotropy magnitude, is plotted with a dotted line for the horizontal models, and a dashed line for the dipping models. Both lines are overlain on the third column for direct comparison. Adjusted R^2 values for the parabolic fits are, from top to bottom: 0.80, 0.93, and 0.97. While all models have similar initial growth rates, with dipping models slightly faster than horizontal, initially horizontal models ultimately out-pace the others, demonstrating that instantaneous linear stability analysis of anisotropic Rayleigh-Taylor dynamics cannot be assumed to apply to time-dependent problems.

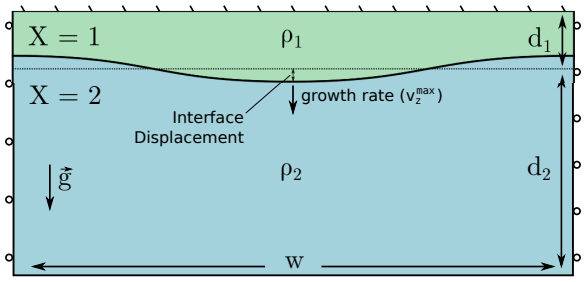

Figure 4.3. Gravitationally unstable model setup with a dense, anisotropic upper layer. We analyze an ensemble of models with various perturbation wavelengths and anisotropy parameters, to investigate Rayleigh-Taylor instabilities in lithosphere modified by aligned igneous intrusions. Model properties are described in the text.

4.5.1 Model setup

Each model in our ensemble has two-dimensional Cartesian geometry with variable width, w, depth, d, and a thin, anisotropic, dense upper domain, underlain by a buoyant, isotropic lower domain, identified by index, X, in model property subscripts (Fig. 4.3). Velocity is fixed (no-slip) on the top, reflecting (free-slip) on the sides, and unconstrained (stress-free) on the bottom.

Model properties are nondimensionalized, following the scaling of Lev and Hager (2008). Total depth is constant, $d = 1$, in all models. The upper domain has density $\rho_1 = 1$, with mean thickness, $d_1 = 0.15$. The lower domain has density $\rho_2 = 0$, and thickness, $d_2 = 0.85$. The model is accelerated by a downward gravitational constant, $g = (0, -1.0)$.

Normal viscosity is constant throughout the model, $\eta_N = 1e - 3$. The upper layer has an initially-uniform anisotropic fabric which is oriented either horizontally (0°), or diagonally (45°), with variable shear viscosity. The lower layer is isotropic in all models, $\eta_S = \eta_N$. The orientation of anisotropy through time obeys equation (4.8), but the magnitude is assumed to remain constant within each fluid.

The fluid interface is vertically perturbed by a sinusoidal function of lateral distance, with amplitude 0.01, and wavelength equal to the model width $\lambda = w$. Wave number is interpreted as a function of the model width, $k = 2\pi/w$. The interface is smoothed in depth to minimize discretization-dependent effects on long-term convective behavior (Bangerth et al., 2017),

$$X = \frac{1}{2}\left[3 + \tanh\left(\frac{z - d_2 - 0.01\cos(2\pi x/w)}{0.005}\right)\right], \tag{4.16}$$

in Cartesian coordinates, x, and z.

Model width, and thus wavenumber, is varied among the ensemble in order to simulate non-integer wavenumbers using finite-width model domains. We discuss this approach in more detail in Appendix B.2.2.

Each model is adaptively refined up to resolution equivalent of 1024×1024 mesh cells (cell geometry ≈ 0.001 high by $w/1025$ wide) near the fluid interface, and as low as 16×16 equivalent elsewhere. Mesh refinement is adjusted every 10 model steps to ensure continuous resolution of the fluid interface. Time step lengths are adaptive, satisfying a Courant number, 1.0. Models are terminated when the fluid interface reaches 45% of the model depth. We vary anisotropy magnitude in the upper layer, $0 \leq 1 - \eta_S/\eta_N \leq 0.95$, and model width, $0.2 \leq w \leq 5$. More information on the numerical implementation is included in Appendix B.

4.5.2 Analysis

Because the time progression of instability depends strongly on effective viscosity, we compare models at equal interface displacements, rather than equal times. That is, we compare snapshots of models taken when the interface perturbation has grown to a particular amplitude, rather than comparing snapshots taken at equal model times. This helps normalize results among models with

different effective viscosities, where one model may have terminated before another has even begun to move significantly.

From each model snapshot, we query both total time elapsed, t, and maximum vertical interface velocity, taken to be the model's instantaneous growth rate, as functions of interface displacement. Model time discretization means that we don't necessarily have snapshots of all models when their fluid interface is displaced by any given amount. By interpolating to a common set of displacement snapshots we can directly compare the progression of instability growth among models (Fig. 4.2).

At each displacement snapshot, we fit a polynomial to growth rate for the entire ensemble. This helps smooth spatial and temporal discretization differences between models, especially significant at low displacement amplitudes. Because the results are best visualized in log space with respect to wave-number and growth rate, we fit a function to the logarithm of both quantities,

$$\log(G) = \Gamma_1 \log(k)^2 + \Gamma_2 \log(k) + \Gamma_3, \tag{4.17}$$

for growth rate, G, with coefficients, Γ_i, as linear functions of anisotropy magnitude in the horizontal and dipping bases,

$$\Gamma_i = \alpha_i H + \beta_i D + \gamma_i \tag{4.18}$$

where α_i, β_i, and γ_i are fit parameters; H and D are magnitudes of horizontal and dipping anisotropy, respectively:

$$H = \begin{cases} 1.0 - \eta_S/\eta_N & \text{if } \theta = 0°, \\ 0 & \text{otherwise,} \end{cases} \tag{4.19}$$

and

$$D = \begin{cases} 1.0 - \eta_S/\eta_N & \text{if } \theta = 45°, \\ 0 & \text{otherwise,} \end{cases} \tag{4.20}$$

where θ is the model's initial anisotropic fabric orientation, relative to horizontal.

We interpret the most unstable wavenumber, k_{max}, as the wavenumber where instantaneous growth rate is highest,

$$\left.\frac{\partial G}{\partial k}\right|_{k_{max}} = 0, \tag{4.21}$$

$$k_{max} = -\frac{\alpha_2 H + \beta_2 D + \gamma_2}{\alpha_1 H + \beta_1 D + \gamma_1}. \tag{4.22}$$

Both growth rate, and k_{max} are shown in Fig. 4.2, projected into the H ($D = 0$), and D ($H = 0$) planes.

4.5.3 Results

Analytic solutions of Lev and Hager (2008) suggest that lithosphere with dipping anisotropy is more unstable than that with horizontal anisotropy. Our results show that this is only true in the early stages of model development, and does not hold for time-evolving systems (Fig. 4.4). In fact, models with initially-horizontal anisotropic fabric significantly out-pace models with dipping initial fabric relatively quickly.

Further, Lev and Hager (2008) find that horizontal anisotropy generates substantially longer wavelength drips than that with dipping anisotropy in the instantaneous limit, $t \rightarrow 0$. We show that this result also cannot be trivially extrapolated to long-term convective behavior. Models with either orientation of initial anisotropy tend to converge over time, becoming more closely aligned with values of the initially-horizontal models.

The rate and dominant wavelength with which instabilities develop in anisotropic models, regardless of their initial orientation, is substantially different than models with isotropic fabric. The existence of anisotropy in any form is much more consequential to potential gravitational instabilities than its orientation.

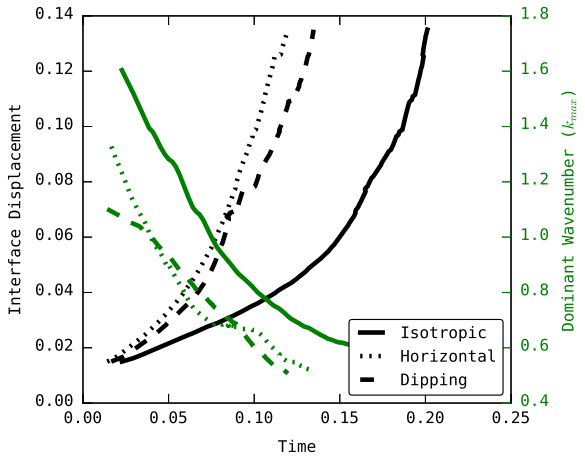

Figure 4.4. Interface displacement of Rayleigh-Taylor instabilities with horizontal, dipping, and isotropic initial fabrics. Horizontal and dipping models have anisotropy magnitude, $1 - \eta_S/\eta_N = 0.9$ in the dense upper layer. The isotropic model has constant viscosity, $\eta_S = \eta_N$. All models demonstrate exponential growth during early stages, followed by super-exponential growth over longer time scales, as is expected for Rayleigh-Taylor instability growth.

4.6 Discussion

Elkins-Tanton and Hager (2000) showed that magmatic intrusions may induce lower-crustal instabilities by crystallizing dense mineral phases. Subsequently, intrusion-triggered delamination has been invoked to explain enigmatic observations from continental magmatic episodes globally, including the Siberian Traps of northern Russia (Elkins-Tanton, 2005), the southern Rocky Mountain ignimbrite flare-up of the Cordilleran U.S. (Farmer et al., 2008), the Columbia River flood basalts of the northwestern U.S. (Camp & Hanan, 2008; Hales et al., 2005), and the Songliao basin of northeastern China (F. Wang et al., 2006). This hypothesis is consistent with geophysical and geochemical observations that are otherwise difficult to reconcile.

The same study found that the ability of such a mechanism to produce gravity-driven instabilities relies on the existence of a weak layer on which dense lower-crust can detach from the buoyant upper-crust (Elkins-Tanton & Hager,

2000), consistent with conclusions drawn from many delamination modeling efforts (Beall et al., 2017; Burov, Guillou-Frottier, d'Acremont, Le Pourhiet, & Cloetingh, 2007; Elkins-Tanton, 2005; Krystopowicz & Currie, 2013). Our results support the conclusion that lithospheric delamination requires weak regions, but suggest an alternative interpretation for their origin. We have shown that molten intrusions can soften the host rock to nearly the viscosity of liquid magma, along certain planes of weakness. Therefore, we suggest that magmatic intrusions themselves may provide the low viscosity layers necessary for efficient lithospheric delamination. This proposed mechanism connects the apparent necessity of mechanically weak layers with prior work on intrusion-delamination-eruption feedbacks.

It should be noted that our lithospheric foundering models assume that fractures extend to the base of the lithosphere. While smooth, continuous fractures are common in the crust, magma transport in the mantle lithosphere is typically more complex (e.g. Holtzman et al., 2003; Keller & Katz, 2016). However, we take the observation from flood basalt eruptions, that episodes of high magma flux can rapidly transport large volumes of melt across the lithosphere, to suggest that lithosphere-scale dikes are a plausible mechanism of magma transport during such atypical events.

Our models also assume that anisotropy magnitude remains constant through time, but the systems we aim to model are dynamic, and material properties evolve with time. In particular, heat transport between host rock and intrusion can modify the viscosity of both, changing the overall magnitude of anisotropy. Heat transfer during pervasive intrusion emplacement causes profound weakening of the host rock (Dufek & Bergantz, 2005; Karlstrom et al., 2017; Karlstrom & Richards, 2011). Conversely, over longer intervals, intrusions become more viscous as they cool and solidify, potentially even surpassing the host rock's

viscosity. In such cases, the system's anisotropy parameters can change drastically through time, but the model's kinematics will still fall within the parameter space mapped in Fig.4.2. Understanding the lithosphere's thermodynamic state through the course of a magmatic episode will be an important future direction of this work.

4.7 Conclusion

We have demonstrated that magmatic intrusions can produce strong anisotropic fabric in rock to which they are emplaced. The magnitude of resulting anisotropy is highly sensitive to the ratio of intrusion viscosity to host rock viscosity. In magmatic systems, this effect may produce anisotropic fabric many orders of magnitude stronger than that generated by other mechanisms.

Dense lithosphere, with even modest reduction in shear viscosity, forms Rayleigh-Taylor instabilities on much shorter timescales than equivalent isotropic lithosphere. Our results suggest that volcanically active regions may be inherently more prone to lithospheric delamination than other areas. This finding is consistent with other studies suggesting that continental volcanism is often associated with delamination events. Thus, we propose that weakening produced by magmatic intrusions may contribute to the rapid acceleration of volcanism seen in many large igneous provinces.

CHAPTER V

CONCLUSION

Here I have presented several interconnected stories for unconventional tectonic processes in the Tertiary Pacific Northwest. While 20^{th} century exploration of the western U.S. led to many pivotal discoveries that underpin modern plate tectonic theory, the Northwest appears frequently to defy the same laws. In some ways, while the plate tectonic revolution contextualized geologic observations around the world, it may have also hindered our understanding of the geologic processes that shape the Pacific Northwest.

Individually, the phenomena presented here are not unique to the Pacific Northwest, but their magnitudes are unusual. This combination of events clustered in time and space around the CRB eruptions, makes the Pacific Northwest arguably the best locality for observing "vertical tectonics" worldwide.

APPENDIX A

ECLOGITE-INDUCED SUBSIDENCE: MODELS

As discussed in Chapter II, we split the conceptual model for eclogite-driven subsidence into two parts: a mechanical part, and a thermochemical part. The mathematical system is similarly split into two sets of coupled equations which we solve with finite difference and finite element methods, respectively. The two models are described below, along with necessary details to reproduce all relevant results and figures.

All code referenced below can be found in the supplemental files included with this dissertation, or in the online supplement to the published version of this work[1]. Documentation of each necessary file is described in the following text.

A.1 Flexure

Eclgite-induced subsidence is discussed at length in the text. Mechanically, it is relatively straightforward, being basically an isostatic adjustment filtered through an elastic plate.

Conceptually, the steps are as follows:

- Lava flows into the CCBD.
- Added weight of new basalt is filtered through the elastic plate to some region of lower crust.
- Some rocks that had been close to garnet stability conditions are able to eclogitize.
- Eclogitization densifies, and thus contracts the lower crust.
- Contraction is elastically filtered back through the crust to the surface, where it is expressed as subsidence.

[1]GSA Data Repository item 2018221, physical and thermo-chemical models of eclogite-induced subsidence, is available online at http://www.geosociety.org/datarepository/2018/ or on request from editing@geosociety.org

In modeling the system, we treat these steps as follows:

- We assume that the pressure of new deposition is transmitted hydrostatically to the lower crust.
- Thus, a volume of lower crust that is exactly the same dimensions, V, as the new lava deposit is converted to eclogite.
- Eclogitization decreases the volume of this lower crustal lens to $V\rho_b/\rho_e$, where ρ_b and ρ_e are the density of basalt and eclogite, respectively.
- We expect this contraction will likewise create $(1 - \rho_b/\rho_e V)$ total subsidence.
- This is equivalent to applying a load of $[\rho_m(1 - \rho_b/\rho_e)g]$ Pascals to the plate, where ρ_m is the density of mantle, and g is gravity.
- We therefore model the contraction as a loading force applied to a buoyantly-supported, thin elastic plate (Equation 2.1).

We vary elastic thickness in the suite models represented in Figure 2.3. All other properties are held constant. Density of basalt, mantle, and eclogite are fixed at 3000, 3300, and 3370 $\mathrm{kg\,m^{-3}}$ respectively (Hacker, 2013). Young's modulus is 7×10^{10} Pa (Li, Dyt, & Griffiths, 2004), and Poisson's ratio is 0.25 (Stüwe, 2007).

A.1.1 Reproducing the Flexure Model

We solve equations 2.1 and 2.2 with a finite difference approximation, written in Python. The model, and all associated code to reproduce Figure 2.3 is in the file `flex.py`. In order to run the model, you must first have Python installed (tested with versions `2.7` and `3.6`), and modules `scipy` (tested with version `1.1.0`) and `matplotlib` (tested with version `2.2.2`). Other versions are not guaranteed to work, but significant changes in these libraries are infrequent, and other versions very well may work. Both module dependencies come standard with most scientific Python distributions, and are packaged in all major Linux distributions. The best way to install the exact versions is through the cross-platform pip package manager:

```
pip install scipy=1.1.0 matplotlib=2.2.2
```

With the above software dependencies satisfied, the model can be run by executing the script:

```
python ./flex.py
```

This will generate Figure 2.3 as shown in the text, and save it as a file (Figure3.tiff) in the working directory.

A.2 Latent Heat

Latent heat release during eclogitization inhibits further reaction. The reaction's positive Clapeyron slope at high temperature means that increased temperature tends to favor spinel stability. Over time, the latent heat diffuses away, permitting further eclogitization. The crux of the problem is a competition between the rate of latent heat release and thermal diffusion. The system is illustrated in Figure A.1, with variables corresponding to those used in the text.

Our governing equations are defined in the main text, equations 2.3 and 2.4. We nondimensionalize the equations before solving to reduce the number of free parameters. We first parameterize temperature as a perturbation to a "reference" geotherm, G: $Gz + T_0 + T'$; and describe the Clapeyron slope in pressure, as a function of temperature: $P_c = \rho \Delta S T + \rho g z_0$. We scale the system by a Péclet number, $Pe_r = \mathbf{U}^3/[\mathbf{\Delta SG}\alpha]$, with variables defined in chapter II:

$$\begin{aligned} \rho' C_p' \left(\frac{\partial T'}{\partial t'} + u' \frac{\partial T'}{\partial z'} \right) - Pe_r^{-1} \frac{\partial}{\partial z'} \left(\rho' C_p' \alpha' \frac{\partial T'}{\partial z'} \right) \\ = \rho' \left(G' z' + T_0' + T' \right) \Delta S' \left(\frac{\partial X'}{\partial t'} + u' \frac{\partial X'}{\partial z'} \right) \end{aligned} \tag{A.1}$$

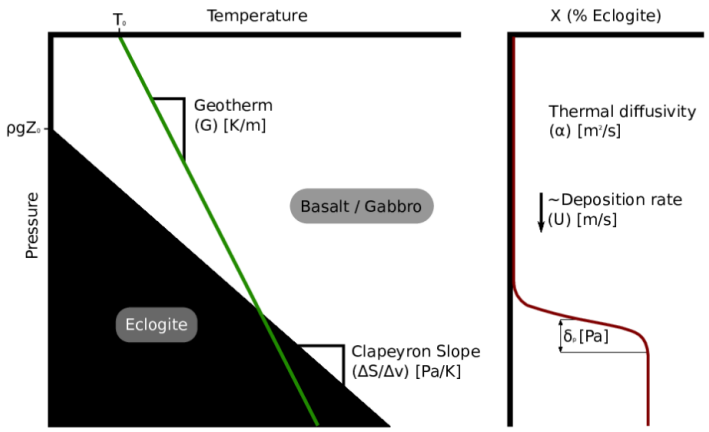

Figure A.1. Conceptual 1D model of surface-load induced eclogitization of lower crust. The background geotherm is advected down at the rate of surface loading. Simultaneously minerals crossing the coexistence curve into the eclogite stability field release latent heat, modifying the thermal profile and inhibiting further eclogitization.

$$\frac{\partial X'}{\partial t'} = A' \exp\left(\frac{-E'_a}{R'(G'A' + T'_0 + T')}\right) \left(\frac{1}{2} + \frac{1}{2}\tanh\left(\frac{z' - z'_0 - (G'z' + T'_0 + T')}{\delta_p}\right) - X'\right) \tag{A.2}$$

where primed variables represent the nondimensional equivalents of those defined in the text.

We solve equations A.1 and A.2 using the TerraFERMA finite element framework (Wilson, Spiegelman, & van Keken, 2017), closely based on the FeniCS project (Logg, Mardal, & Wells, 2012). This allows us to define our entire model in two, self-contained, and portable parameter files (latent_heat.tfml, and latent_heat.shml). This approach is highly reproducible, and our code may be (relatively) easily audited by any interested reader. Details on how to do so are described below.

Results are shown in Figure A.2 for a range of Péclet numbers, and demonstrate that for $Pe >> 1$, the eclogite conversion is spread over a wide range

of depths, and rocks may never fully metamorphose within the model domain. However, for realistic geologic scenarios, $Pe << 1$. At low Péclet numbers the model converges to the limiting case where heat diffuses infinitely quickly. That is, latent heat released by eclogitization is diffused away much faster than new basalt is advected through the system.

A.2.1 Reproducing the Latent Heat Model

TerraFERMA is available under a free and open source license at https://terraferma.github.io/. The simplest method to reproduce Figure A.2 is to run TerraFERMA with Docker, rather than installing it locally. You can get Docker from https://docs.docker.com/engine/getstarted/step_one/.

Once you have installed Docker, `cd` to the directory containing the `.tfml` and `.shml` files, and run the model with the following command:

```
docker run -v "$PWD:/home/tfuser/shared" --rm terraferma/dev
↪  'source /etc/profile; source .profile; cd shared/;
↪  tfsimulationharness --test latent_heat.shml' -u tfuser
```

This will start a Docker image with TerraFERMA pre-installed and configured. It will then compile and run the model. It will place the resulting plots in the current directory.

The flags in the above command tell docker to share the current directory from your computer with the container (`-v "$PWD:/home/tfuser/shared"`) and to clean up the container when the model is done running (`--rm`). The argument (`terraferma/dev`) is the name of the container. If the TerraFERMA container is not already on your system (which it probably isn't if you're following these instructions for the first time), Docker will automatically download it. The long line in single quotes is the actual

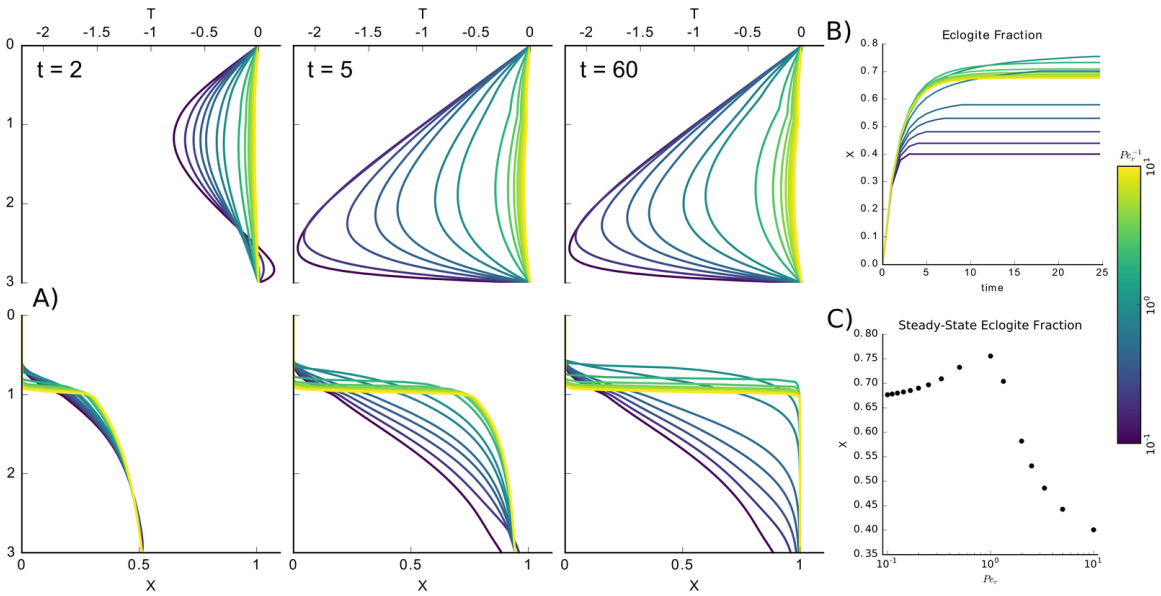

Figure A.2. Solutions to equation A.1 and A.2 for various Péclet numbers over time until steady state. Thermal boundary conditions are imposed at the top and bottom of the model, forcing the temperature to start and end at the reference geotherm. Eclogite is constrained to zero at the top of the model. Temperature is initialized to match the reference geotherm, and eclogite is initialized to zero everywhere. **A**: Top row shows nondimensional temperature perturbations over time for models with a range of Péclet numbers. Lighter colors represent low Péclet values. We can see that the low Péclet system stays close to the reference geotherm throughout the model run. High Péclet models diverge from the reference geotherm, cooling due to cold upper crust advecting to depth more quickly than heat can diffuse to reestablish the geotherm. There is a noticeable kink in the temperature solution for the intermediate Péclet systems where eclogite first begins to form. The bottom row shows eclogite fraction over time for the same models as in the top row. All models start with no eclogite, and develop eclogite over time. The low Péclet systems quickly move to establish a equilibrium eclogite profile, with the deeper, hotter parts achieving equilibrium more quickly owing to the thermal dependence of reaction rate in equation A.2. **B**: Integrated eclogite fraction for each model over time. **C**: Steady-state integrated eclogite fraction as a function of Péclet number. We can see that for very low Pe_r, this value trends towards the prescribed equilibrium value of 66%. As Pe_r increases, the total eclogite fraction increases, because advective cooling shallows the depth to eclogite stability. At very high Pe_r, rocks advect all the way through the model domain without fully reacting, represented by a decrease in total eclogite within the model. There is a peak at Pe_r=1 where these competing effects trade off most efficiently for eclogite formation. In this case the integrated eclogite fraction is $>$ 75%. It's worth noting that for any reasonable values of **U**, **ΔS**, **G**, and $\mathbf{Pe_r}$ is very very low. Only the low Pe_r limit is applicable to geologic problems, including eclogite-driven subsidence.

command that will execute inside the container. It initializes some UNIX environment variables (`source /etc/profile; source .profile`), moves to the shared directory (`cd shared/`), and finally compiles and executes the TerraFerma model, including postprocessing 'tests' that generate figures (`tfsimulationharness --test latent_heat.shml`). The final flag tells docker to run the above command as the user, `tfuser`, in the container environment (`-u tfuser`).

Figure A.2 was generated with terraferma/dev container v1.0, build code: `bhpnedhtezj48dcagpzsdye`.

A.2.2 Modifying the Latent Heat Model

TerraFERMA options files (.tfml and .shml) are in XML format, and meant to be read by the `SPUD` options processing system (Ham et al., 2008). Because the files are plain text, it is possible to modify them with a text editor, but for any significant changes, the best way to modify the model is with `SPUD`'s official GUI, *Diamond*. More information can be found on running Diamond on the TerraFERMA wiki (https://github.com/TerraFERMA/TerraFERMA). If one only wants to audit the equations, the relevant parameters can be found in lines 229 – 248 of the file `latent_heat.tfml`, and may be checked with a text editor.

APPENDIX B

ANISOTROPIC VISCOSITY: NUMERICAL IMPLEMENTATION

B.1 Equations

To enable anisotropic viscosity in ASPECT, we substitute the scalar viscosity, η, with a symmetric fourth-order tensor, C_{ijkl}, representing an arbitrary linear map from strain rate to deviatoric stress. The full momentum balance equation solved by ASPECT is extended to

$$2\left(C_{ijkl}\dot{\varepsilon}_{kl} - \frac{1}{3}(C_{iikl}\dot{\varepsilon}_{kl}\delta_{ij})\right)_{,j} - p\delta_{ij} + \rho g_i = 0. \tag{B.1}$$

We modify the viscous heating term in ASPECT's thermal advection-diffusion equation accordingly,

$$\begin{aligned}\rho C_p\left(T_{,t} + u_i T_{,i}\right) - \left(\rho C_p \kappa T_{,i}\right)_{,i} &= \ldots \\ +2\left(C_{ijkl}\dot{\varepsilon}_{kl} - \frac{1}{3}(C_{iikl}\dot{\varepsilon}_{kl}\delta_{ij})\right) &: \left(\dot{\varepsilon}_{ij} - \frac{1}{3}u_{i,i}\delta_{ij}\right) \\ &+ \ldots\end{aligned} \tag{B.2}$$

The full equations are more general than the scope of this work. Specifically, in the models presented above, we assume the fluid is incompressible, and we do not consider temperature diffusion. The extra terms are shown here, and included in the supplementary code, for completeness.

We track spatially variable quantities with $dim + 3$ additional fields that advect with the fluid velocity, where dim is the model's spatial dimension. All of the models in this paper are 2-dimensional ($dim = 2$), but the model can be trivially extended to 3-D.

ASPECT is agnostic to the purpose of the compositional fields, and only modifies them while solving equation (4.3). Our code is implemented as a plug-in to ASPECT that interprets these fields as: model domain, X; shear viscosity, η_S; normal viscosity, η_N; and n_i, the dim components of director vector, respectively. It

returns coefficients for the governing equations:

$$C_{ijkl} = \eta_N \mathbf{1} - (\eta_N - \eta_S)\Lambda_{ijkl}, \tag{B.3}$$

with fourth-order identity tensor, $\mathbf{1}$, director tensor Λ, as defined in equation (4.7); density,

$$\rho = \begin{cases} 1 & \text{if } X = 1, \\ 0 & \text{if } X = 2; \end{cases} \tag{B.4}$$

and source/sink terms for equation (4.3), which simulate the time-dependent variation of n_i, via equation (4.8),

$$q_i = \dot{n}_i. \tag{B.5}$$

B.2 Validation

We perform several validations of our implementation.

B.2.1 Method of manufactured solutions

First, we verify that we are accurately solving the governing equations by testing convergence to a manufactured solution (Roy, 2005).

Beginning with known velocity solution,

$$u = \left(\sin(2y)\sin(2x), \left(\cos(2y) + 1\right)\cos(2x)\right), \tag{B.6}$$

and constitutive tensor, C_{ijkl}, representing a uniform anisotropic fluid, we manually solve equation (4.1) for ρg_i. Equation (B.6) was chosen because it isolates simple shear, and pure shear within the same model domain.

We impose the derived body force in an identical ASPECT model, and invert for velocity, expecting our solution to equal the known solution (Eq. B.6). Pressure is constrained to zero everywhere, in order to isolate the velocity components of our solution. We compute the model error as the difference between the numerical

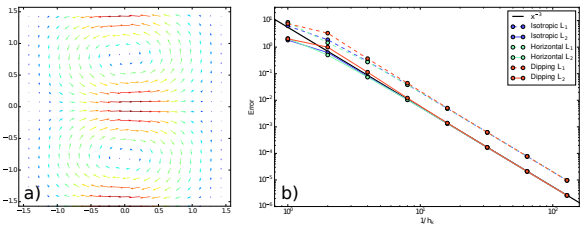

Figure B.1. Convergence to a manufactured solution demonstrates expected accuracy of finite element solver. **A**: Analytically defined velocity field, chosen to isolate both pure shear and simple shear. **B**: Reduction of model error relative to analytic solution as a function of mesh cell size, h, in both L_1 and L_2 norms.

solution, and the analytic one in the L_1 and L_2 norms, as a function of mesh size, h. Our implementation converges with the expected order, $\mathcal{O}(h^3)$ (Kronbichler et al., 2012), in both norms (Fig. B.1).

B.2.2 Rayleigh-Taylor growth

We further validate our model against the analytic solutions of Lev and Hager (2008). The model setup is identical to that described in Section 4.5.1, where the anisotropic models have magnitude 0.9. We solve equations (4.1) and (4.2), once for each model. In each case, we interpret the average vertical velocity along the fluid interface as the instability growth rate. Our solutions align well with analytic solutions (Fig. B.2).

We tested several approaches to reproduce these solutions. Our initial attempts were based on a single model for each anisotropy orientation, in which we perturbed the fluid interface by many frequencies, and attempted to measure the growth rate and dominant frequency. This method proved difficult both because of numerical discretization limitations which make superimposed perturbations difficult to resolve, and the constraint that finite-width model domains can only contain integer wavenumbers, which limits generality of the solutions. Further, the maximum instability wavenumber, k_{max}, becomes difficult to define over finite-time,

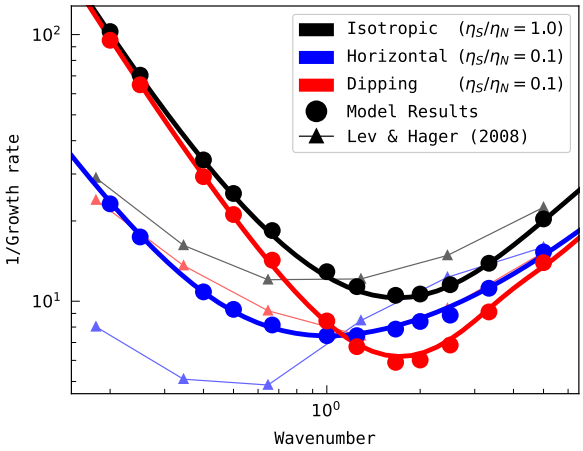

Figure B.2. Rayleigh-Taylor instability growth rates from our numerical models (dots) compare well with analytic solutions of Lev and Hager (2008) (thick lines). Our solutions show a significant model fit improvement over previous numerical implementations (triangles), especially at low wavenumbers.

where the interface undergoes significant deformation, which would make this test less relevant to our finite-time models, discussed in the main text.

Our results are substantially closer to the analytic solution than those of Lev and Hager (2008), possibly owing to the specifics of our model setup. In particular, the method described above, of perturbing the interface with a single frequency per model, and varying the model width across many runs, seemed to result in the single most significant improvement over other methods we tried.

REFERENCES CITED

Ahrens, T. J., & Schubert, G. (1975, May). Gabbro-eclogite reaction rate and its geophysical significance. *Rev. Geophys.*, *13*(2), 383-400. doi: 10.1029/RG013i002p00383

Allen, J. E. (1991, September). The case of the inverted auriferous paleotorrent–exotic quartzite gravels on Wallowa Mountain peaks. *Or. Geol.*, *53*(5), 104-107. Retrieved 2018-11-11, from `https://www.oregongeology.org/pubs/og/OGv53n05.pdf`

Backus, G. E. (1962, October). Long-wave elastic anisotropy produced by horizontal layering. *Journal of Geophysical Research*, *67*(11), 4427-4440. doi: 10.1029/JZ067i011p04427

Bangerth, W., Dannberg, J., Gassmöller, R., Heister, T., & others. (2017, April). ASPECT*: Advanced Solver for Problems in Earth's ConvecTion, User manual.* doi: 10.6084/m9.figshare.4865333

Barry, T., Kelley, S., Reidel, S., Camp, V., Self, S., Jarboe, N., … Renne, P. (2013, August). Eruption chronology of the Columbia River Basalt Group. In *Geological Society of America Special Papers* (Vol. 497, p. 45-66). Geological Society of America. doi: 10.1130/2013.2497(02)

Beall, A. P., Moresi, L., & Stern, T. (2017). Dripping or delamination? A range of mechanisms for removing the lower crust or lithosphere. *Geophys J Int.* doi: 10.1093/gji/ggx202

Burns, E. R., Morgan, D. S., Peavler, R. S., & Kahle, S. C. (2011, February). *Three-dimensional model of the geologic framework for the Columbia Plateau regional aquifer system, Idaho, Oregon, and Washington* (Tech. Rep. No. 2010-5246). U.S. Geological Survey Groundwater Resources Program. doi: 10.3133/sir20105246

Burov, E., Guillou-Frottier, L., d'Acremont, E., Le Pourhiet, L., & Cloetingh, S. (2007, April). Plume head–lithosphere interactions near intra-continental plate boundaries. *Tectonophysics*, *434*(1), 15-38. doi: 10.1016/j.tecto.2007.01.002

Camp, V. E., & Hanan, B. B. (2008, June). A plume-triggered delamination origin for the Columbia River Basalt Group. *Geosphere*, *4*(3), 480-495. doi: 10.1130/GES00175.1

Campbell, N. (1989). Structural and stratigraphic interpretation of rocks under the Yakima fold belt, Columbia Basin, based on recent surface mapping and well data. In S. P. Reidel & P. R. Hooper (Eds.), *Volcanism and Tectonism in the Columbia River Flood-basalt Province* (p. 209-222). Boulder, Colo: Geological Society of America.

Carson, R. J., & Spencer, P. K. (1995). The Enterprise Gravel: The Ancestral Wallowa River and neotectonism in Northeastern Oregon. *Northwest Sci.*, *69*(1), 60-71. Retrieved from `http://hdl.handle.net/2376/1330`

Catchings, R. D., & Mooney, W. D. (1988, January). Crustal structure of the Columbia Plateau: Evidence for continental rifting. *J. Geophys. Res.*, *93*(B1), 459-474. doi: 10.1029/JB093iB01p00459

Christensen, R. M. (2005). *Mechanics of composite materials*. Dover Publications.

Christensen, U. R. (1987, December). Some geodynamical effects of anisotropic viscosity. *Geophys. J. R. Astron. Soc.*, *91*(3), 711-736. doi: 10.1111/j.1365-246X.1987.tb01666.x

Christiansen, R. L., & Yeats, R. S. (1992). Post-Laramide geology of the U.S. Cordilleran region. In B. C. Burchfiel, P. W. Lipman, & M. L. Zoback (Eds.), *The Cordilleran Orogen: Conterminous U.S.* (Vol. G-3, p. 261-406). Boulder, Colo: Geological Society of America.

Conrad, C. P., & Molnar, P. (1997, April). The growth of Rayleigh–Taylor-type instabilities in the lithosphere for various rheological and density structures. *Geophys. J. Int.*, *129*(1), 95-112. doi: 10.1111/j.1365-246X.1997.tb00939.x

Crampin, S. (1978, June). Seismic-wave propagation through a cracked solid: Polarization as a possible dilatancy diagnostic. *Geophys J Int*, *53*(3), 467-496. doi: 10.1111/j.1365-246X.1978.tb03754.x

Dannberg, J., & Heister, T. (2016, December). Compressible magma/mantle dynamics: 3-D, adaptive simulations in ASPECT. *Geophys J Int*, *207*(3), 1343-1366. doi: 10.1093/gji/ggw329

Darold, A., & Humphreys, E. (2013, March). Upper mantle seismic structure beneath the Pacific Northwest: A plume-triggered delamination origin for the Columbia River flood basalt eruptions. *Earth and Planetary Science Letters*, *365*, 232-242. doi: 10.1016/j.epsl.2013.01.024

Dorsey, R. J., & LaMaskin, T. A. (2008). Mesozoic collision and accretion of oceanic terranes in the Blue Mountains Province of northeastern Oregon: New insights from the stratigraphic record. In J. E. Spencer & S. R. Titley (Eds.), *Arizona Geological Society Digest 22* (Vol. 22, pp. 325–332). Tuscon, Arizona. Retrieved 2018-11-28, from `http://pages.uoregon.edu/rdorsey/Downloads/Dorsey&LaMaskin2008.pdf`

Dufek, J., & Bergantz, G. W. (2005, July). Lower crustal magma genesis and preservation: A stochastic framework for the evaluation of basalt–crust interaction. *J Petrology*, *46*(11), 2167-2195. doi: 10.1093/petrology/egi049

Elkins-Tanton, L. T. (2005, January). Continental magmatism caused by lithospheric delamination. *Geological Society of America Special Papers*, *388*, 449-461. doi: 10.1130/0-8137-2388-4.449

Elkins-Tanton, L. T. (2007, March). Continental magmatism, volatile recycling, and a heterogeneous mantle caused by lithospheric gravitational instabilities. *J. Geophys. Res.*, *112*(B3), B03405. doi: 10.1029/2005JB004072

Elkins-Tanton, L. T., & Hager, B. H. (2000, December). Melt intrusion as a trigger for lithospheric foundering and the eruption of the Siberian flood basalts. *Geophysical Research Letters*, *27*(23), 3937-3940. doi: 10.1029/2000GL011751

Farmer, G. L., Bailley, T., & Elkins-Tanton, L. T. (2008, April). Mantle source volumes and the origin of the mid-Tertiary ignimbrite flare-up in the southern Rocky Mountains, western U.S. *Lithos*, *102*(1–2), 279-294. doi: 10.1016/j.lithos.2007.08.014

Fischer, K. M. (2002, June). Waning buoyancy in the crustal roots of old mountains. *Nature*, *417*(6892), 933-936. doi: 10.1038/nature00855

Gac, S., Huismans, R. S., Simon, N. S. C., Podladchikov, Y. Y., & Faleide, J. I. (2013, December). Formation of intracratonic basins by lithospheric shortening and phase changes: A case study from the ultra-deep East Barents Sea basin. *Terra Nova*, *25*(6), 459-464. doi: 10.1111/ter.12057

Gao, H., Humphreys, E. D., Yao, H., & van der Hilst, R. D. (2011, April). Crust and lithosphere structure of the northwestern U.S. with ambient noise tomography: Terrane accretion and Cascade arc development. *Earth and Planetary Science Letters*, *304*(1–2), 202-211. doi: 10.1016/j.epsl.2011.01.033

Gaschnig, R. M., Vervoort, J. D., Lewis, R. S., & McClelland, W. C. (2010, June). Migrating magmatism in the northern US Cordillera: In situ U–Pb geochronology of the Idaho batholith. *Contrib Mineral Petrol*, *159*(6), 863-883. doi: 10.1007/s00410-009-0459-5

Gassmöller, R., Heien, E., Puckett, E. G., & Bangerth, W. (2016, December). Flexible and scalable particle-in-cell methods for massively parallel computations. *ArXiv161203369 Phys.*. Retrieved 2018-08-23, from `http://arxiv.org/abs/1612.03369`

Gittings, F. W. (2008, October). *Geological report on the Muskox Property* (Tech. Rep. No. NTS 86 O/6). Coppermine River Area, Nunavut: Platinex Inc. Retrieved 2011-07-15, from `http://www.platinex.com/docs/MuskoxQualifyingReport2008.pdf`

Göğüş, O. H., & Pysklywec, R. N. (2008, November). Near-surface diagnostics of dripping or delaminating lithosphere. *J. Geophys. Res.*, *113*(B11), B11404. doi: 10.1029/2007JB005123

Hacker, B. R. (2013, March). Eclogite formation and the rheology, buoyancy, seismicity, and H2O content of oceanic crust. *Subduction Top Bottom*. doi: 10.1029/GM096p0337

Hales, T. C., Abt, D. L., Humphreys, E. D., & Roering, J. J. (2005, December). A lithospheric instability origin for Columbia River flood basalts and Wallowa Mountains uplift in northeast Oregon. *Nature*, *438*(7069), 842-845. doi: 10.1038/nature04313

Ham, D. A., Farrell, P. E., Gorman, G. J., Maddison, J. R., Wilson, C. R., Kramer, S. C., … Piggott, M. D. (2008, July). Spud 1.0: Generalising and automating the user interfaces of scientific computer models. *Geosci. Model Dev. Discuss.*, *1*(1), 125-146. doi: 10.5194/gmdd-1-125-2008

Hamdani, Y., Mareschal, J.-C., & Arkani-Hamed, J. (1994, March). Phase change and thermal subsidence of the Williston basin. *Geophys J Int*, *116*(3), 585-597. doi: 10.1111/j.1365-246X.1994.tb03282.x

Hansen, L. N., Warren, J. M., Zimmerman, M. E., & Kohlstedt, D. L. (2016, July). Viscous anisotropy of textured olivine aggregates, part 1: Measurement of the magnitude and evolution of anisotropy. *Earth Planet. Sci. Lett.*, *445*, 92-103. doi: 10.1016/j.epsl.2016.04.008

Hansen, L. N., Zimmerman, M. E., & Kohlstedt, D. L. (2012, December). Laboratory measurements of the viscous anisotropy of olivine aggregates. *Nature*, *492*(7429), 415-418. doi: 10.1038/nature11671

Hashin, Z. (1983, September). Analysis of composite materials—a survey. *Journal of Applied Mechanics*, *50*(3), 481-505. doi: 10.1115/1.3167081

Heister, T., Dannberg, J., Gassmöller, R., & Bangerth, W. (2017, August). High accuracy mantle convection simulation through modern numerical methods – II: Realistic models and problems. *Geophys J Int*, *210*(2), 833-851. doi: 10.1093/gji/ggx195

Hirth, G., & Kohlstedt, D. (2003). Rheology of the upper mantle and the mantle wedge: A view from the experimentalists. In J. Eiler (Ed.), *Inside the subduction Factory* (Vol. 138, pp. 83–105). American Geophysical Union. doi: 10.1029/138GM06

Holtzman, B. K., Kohlstedt, D. L., Zimmerman, M. E., Heidelbach, F., Hiraga, T., & Hustoft, J. (2003, August). Melt segregation and strain partitioning: Implications for seismic anisotropy and mantle flow. *Science*, *301*(5637), 1227-1230. doi: 10.1126/science.1087132

Honda, S. (1986, December). Strong anisotropic flow in a finely layered asthenosphere. *Geophys. Res. Lett.*, *13*(13), 1454-1457. doi: 10.1029/GL013i013p01454

Hou, G. (2012, March). Mechanism for three types of mafic dyke swarms. *Geoscience Frontiers*, *3*(2), 217-223. doi: 10.1016/j.gsf.2011.10.003

Houseman, G. A., McKenzie, D. P., & Molnar, P. (1981). Convective instability of a thickened boundary layer and its relevance for the thermal evolution of continental convergent belts. *Journal of Geophysical Research: Solid Earth*, *86*(B7), 6115-6132. doi: 10.1029/JB086iB07p06115

Humphreys, E. D. (1995, November). Post-Laramide removal of the Farallon slab, western United States. *Geology*, *23*(11), 987-990. doi: 10/cqr48r

Ito, K., & Kennedy, G. C. (1971). An experimental study of the basalt-garnet granulite-eclogite transition. In J. G. Heacock (Ed.), *The structure and physical properties of the Earth's crust* (p. 303-314). American Geophysical Union. doi: 10.1029/GM014p0303

Karlstrom, L., Paterson, S. R., & Jellinek, A. M. (2017, July). A reverse energy cascade for crustal magma transport. *Nat. Geosci.*, *10*(8), 604-608. doi: 10.1038/ngeo2982

Karlstrom, L., & Richards, M. (2011, August). On the evolution of large ultramafic magma chambers and timescales for flood basalt eruptions. *J. Geophys. Res.*, *116*(B8), B08216. doi: 10.1029/2010JB008159

Kasbohm, J., & Schoene, B. (2018, September). Rapid eruption of the Columbia River flood basalt and correlation with the mid-Miocene climate optimum. *Sci. Adv.*, *4*(9), eaat8223. doi: 10.1126/sciadv.aat8223

Kay, R., & Kay, S. (1993, March). Delamination and delamination magmatism. *Tectonophysics*, *219*(1-3), 177-189. doi: 10.1016/0040-1951(93)90295-U

Kays, M. A., Stimac, J. P., & Goebel, P. M. (2006). Permian-Jurassic growth and amalgamation of the Wallowa composite terrane, northeastern Oregon. In A. Snoke & C. Barnes (Eds.), *Geological studies in the Klamath Mountains Province, California and Oregon: A volume in honor of William P. Irwin* (Vol. 410, p. 465). Boulder, Colorado: Geological Society of America. Retrieved from `https://doi.org/10.1130/2006.2410(23)` doi: 10.1130/2006.2410(23)

Keller, T., & Katz, R. F. (2016, June). The role of volatiles in reactive melt transport in the asthenosphere. *J. Petrol.*, *57*(6), 1073-1108. doi: 10.1093/petrology/egw030

Keller, T., May, D. A., & Kaus, B. J. P. (2013, January). Numerical modelling of magma dynamics coupled to tectonic deformation of lithosphere and crust. *Geophys. J. Int.*, *195*(3), 1406-1442. doi: 10.1093/gji/ggt306

Kendall, J.-M., & Silver, P. G. (1998). Investigating causes of D″ anistropy. *Core-Mantle Bound. Reg.*. doi: 10.1029/GD028p0097

Kronbichler, M., Heister, T., & Bangerth, W. (2012, January). High accuracy mantle convection simulation through modern numerical methods. *Geophys. J. Int.*, *191*(1), 12-29. doi: 10.1111/j.1365-246X.2012.05609.x

Kruckenberg, S. C., Whitney, D. L., Teyssier, C., Fanning, C. M., & Dunlap, W. J. (2008, July). Paleocene-Eocene migmatite crystallization, extension, and exhumation in the hinterland of the northern Cordillera: Okanogan dome, Washington, USA. *GSA Bulletin*, *120*(7-8), 912-929. doi: 10.1130/B26153.1

Krystopowicz, N. J., & Currie, C. A. (2013, January). Crustal eclogitization and lithosphere delamination in orogens. *Earth and Planetary Science Letters*, *361*, 195-207. doi: 10.1016/j.epsl.2012.09.056

LeCheminant, A. N., & Heaman, L. M. (1989, December). Mackenzie igneous events, Canada: Middle Proterozoic hotspot magmatism associated with ocean opening. *Earth and Planetary Science Letters*, *96*(1), 38-48. doi: 10.1016/0012-821X(89)90122-2

Lev, E., & Hager, B. H. (2008, January). Rayleigh–Taylor instabilities with anisotropic lithospheric viscosity. *Geophys. J. Int.*, *173*(3), 806-814. doi: 10.1111/j.1365-246X.2008.03731.x

Li, F., Dyt, C., & Griffiths, C. (2004, November). 3D modelling of flexural isostatic deformation. *Computers & Geosciences*, *30*(9), 1105-1115. doi: 10.1016/j.cageo.2004.08.005

Liu, L., & Stegman, D. R. (2012, February). Origin of Columbia River flood basalt controlled by propagating rupture of the Farallon slab. *Nature*, *482*(7385), 386-389. doi: 10.1038/nature10749

Logg, A., Mardal, K.-A., & Wells, G. (Eds.). (2012). *Automated solution of differential equations by the finite element method: The FEniCS Book* (1st ed.) (No. 84). Springer-Verlag Berlin Heidelberg. doi: 10.1007/978-3-642-23099-8

Lowry, A. R., & Pérez-Gussinyé, M. (2011). The role of crustal quartz in controlling Cordilleran deformation. *Nature*, *471*(7338), 353. doi: 10.1038/nature09912

McKenzie, D. (1984, August). The Generation and Compaction of Partially Molten Rock. *J. Petrol.*, *25*(3), 713-765. doi: 10.1093/petrology/25.3.713

Michibayashi, K., & Mainprice, D. (2004, February). The role of pre-existing mechanical anisotropy on shear zone development within oceanic mantle lithosphere: An example from the Oman ophiolite. *J Petrology*, *45*(2), 405-414. doi: 10.1093/petrology/egg099

Moore, M. M., Garnero, E. J., Lay, T., & Williams, Q. (2004, February). Shear wave splitting and waveform complexity for lowermost mantle structures with low-velocity lamellae and transverse isotropy. *Journal of Geophysical Research: Solid Earth*, *109*(B2). doi: 10.1029/2003JB002546

Mühlhaus, H.-B., Moresi, L., Hobbs, B., & Dufour, F. (2002, August). Large amplitude folding in finely layered viscoelastic rock structures. *Pure appl. geophys.*, *159*(10), 2311-2333. doi: 10.1007/s00024-002-8737-4

Naimark, B. M., & Ismail-Zadeh, A. T. (1995, October). Numerical models of a subsidence mechanism in intracratonic basins: Application to North American basins. *Geophys. J. Int.*, *123*(1), 149-160. doi: 10.1111/j.1365-246X.1995.tb06667.x

O'Connell, R. J., & Wasserburg, G. J. (1972, February). Dynamics of submergence and uplift of a sedimentary basin underlain by a phase-change boundary. *Rev. Geophys.*, *10*(1), 335-368. doi: 10.1029/RG010i001p00335

O'Driscoll, L. J., & Johnson, K. (2008, October). Geochemical evidence for a dense mafic root of units in the Wallowa Batholith, Wallowa Mountains, northeast Oregon. In *Geological Society of America Abstracts with Programs* (Vol. 40, p. 544). Geological Society of America. Retrieved 2018-11-06, from `https://gsa.confex.com/gsa/2008AM/finalprogram/abstract_146360.htm`

Perry-Houts, J., & Humphreys, E. (2018, July). Eclogite-driven subsidence of the Columbia Basin (Washington State, USA) caused by deposition of Columbia River Basalt. *Geology*, *46*(7). doi: 10.1130/G40328.1

Perry-Houts, J., & Karlstrom, L. (2018, October). Anisotropic viscosity and time-evolving lithospheric instabilities due to aligned igneous intrusions. *Geophys J Int*. doi: 10.1093/gji/ggy466

Reidel, S. P., Camp, V. E., Tolan, T. L., & Martin, B. S. (2013, August). The Columbia River flood basalt province: Stratigraphy, areal extent, volume, and physical volcanology. In *Geological Society of America Special Papers* (Vol. 497, p. 1-43). Geological Society of America. doi: 10.1130/2013.2497(01)

Reidel, S. P., Tolan, T. L., Hooper, P. R., Beeson, M. H., Fecht, K. R., Bentley, R. D., & Anderson, J. L. (1989). The Grande Ronde Basalt, Columbia River Basalt Group; Stratigraphic descriptions and correlations in Washington, Oregon, and Idaho. In S. P. Reidel & P. R. Hooper (Eds.), *Volcanism and Tectonism in the Columbia River Flood-basalt Province* (p. 21-54). Boulder, Colo: Geological Society of America.

Richter, F. M., & Daly, S. F. (1978, October). Convection models having a multiplicity of large horizontal scales. *J. Geophys. Res.*, *83*(B10), 4951-4956. doi: 10.1029/JB083iB10p04951

Roy, C. J. (2005, May). Review of code and solution verification procedures for computational simulation. *Journal of Computational Physics*, *205*(1), 131-156. doi: 10.1016/j.jcp.2004.10.036

Ryan, W. B., Carbotte, S. M., Coplan, J. O., O'Hara, S., Melkonian, A., Arko, R., … others (2009). Global multi-resolution topography synthesis. *Geochem. Geophys. Geosystems*, *10*(3). doi: 10.1029/2008GC002332

Saito, M., & Abe, Y. (1984). Consequences of anisotropic viscosity in the Earth's mantle. *Zisin J. Seismol. Soc. Jpn. 2nd Ser*, *37*(2), 237-245. doi: 10.4294/zisin1948.37.2_237

Saleeby, J., Ducea, M., & Clemens-Knott, D. (2003, December). Production and loss of high-density batholithic root, southern Sierra Nevada, California. *Tectonics*, *22*(6), 1064. doi: 10.1029/2002TC001374

Schmalholz, S. M., & Podladchikov, Y. Y. (2001, October). Strain and competence contrast estimation from fold shape. *Tectonophysics*, *340*(3), 195-213. doi: 10.1016/S0040-1951(01)00151-2

Schwartz, J. J., Snoke, A. W., Cordey, F., Johnson, K., Frost, C. D., Barnes, C. G., … Wooden, J. L. (2011, September). Late Jurassic magmatism, metamorphism, and deformation in the Blue Mountains Province, northeast Oregon. *GSA Bulletin*, *123*(9-10), 2083-2111. doi: 10.1130/B30327.1

Stüwe, K. (2007). *Geodynamics of the lithosphere: An introduction*. Springer Science & Business Media.

Tandon, G. P., & Weng, G. J. (1984). The effect of aspect ratio of inclusions on the elastic properties of unidirectionally aligned composites. *Polymer Composites*, *5*(4), 327-333. doi: 10.1002/pc.750050413

Taubeneck, W. H. (1970). Dikes of Columbia River Basalt in northeastern Oregon, western Idaho, and southeastern Washington. In E. H. Gilmour & D. Stradling (Eds.), *Proceedings of the second Columbia River Basalt Symposium* (p. 73-96). Cheney, Washington: Eastern Washington State College Press.

Taylor, S. B., Johnson, S. Y., Fraser, G. T., & Roberts, J. W. (1988, July). Sedimentation and tectonics of the lower and middle Eocene Swauk Formation in eastern Swauk Basin, central Cascades, central Washington. *Can. J. Earth Sci.*, *25*(7), 1020-1036. doi: 10.1139/e88-100

Thompson, R. N., & Gibson, S. A. (1991, November). Subcontinental mantle plumes, hotspots and pre-existing thinspots. *J. Geol. Soc.*, *148*(6), 973-977. doi: 10.1144/gsjgs.148.6.0973

Tommasi, A., Knoll, M., Vauchez, A., Signorelli, J. W., Thoraval, C., & Logé, R. (2009, June). Structural reactivation in plate tectonics controlled by olivine crystal anisotropy. *Nat. Geosci.*, *2*(6), 423-427. doi: 10.1038/ngeo528

Turcotte, D., & Schubert, G. (2014). *Geodynamics* (3rd ed.). Cambridge University Press.

Vauchez, A., Tommasi, A., & Barruol, G. (1998, October). Rheological heterogeneity, mechanical anisotropy and deformation of the continental lithosphere. *Tectonophysics*, *296*(1), 61-86. doi: 10.1016/S0040-1951(98)00137-1

Wang, F., Zhou, X.-H., Zhang, L.-C., Ying, J.-F., Zhang, Y.-T., Wu, F.-Y., & Zhu, R.-X. (2006, November). Late Mesozoic volcanism in the Great Xing'an Range (NE China): Timing and implications for the dynamic setting of NE Asia. *Earth Planet. Sci. Lett.*, *251*(1-2), 179-198. doi: 10.1016/j.epsl.2006.09.007

Wang, H., & Currie, C. A. (2017, August). Crustal deformation induced by mantle dynamics: Insights from models of gravitational lithosphere removal. *Geophys J Int*, *210*(2), 1070-1091. doi: 10.1093/gji/ggx209

Wendt, A. S., Mainprice, D., Rutter, E., & Wirth, R. (1998, August). A joint study of experimental deformation and experimentally induced microstructures of pretextured peridotites. *J. Geophys. Res.*, *103*(B8), 18205-18221. doi: 10.1029/98JB01555

Wilson, C. R., Spiegelman, M., & van Keken, P. E. (2017). TerraFERMA: The Transparent Finite Element Rapid Model Assembler for multiphysics problems in Earth sciences. *Geochem. Geophys. Geosyst.*, 769-810. doi: 10.1002/2016GC006702

Wolff, J. A., Ramos, F. C., Hart, G. L., Patterson, J. D., & Brandon, A. D. (2008, March). Columbia River flood basalts from a centralized crustal magmatic system. *Nature Geosci*, *1*(3), 177-180. doi: 10.1038/ngeo124

Wyld, S. J., & Wright, J. E. (2001, January). New evidence for Cretaceous strike-slip faulting in the United States Cordillera and implications for terrane-displacement, deformation patterns, and plutonism. *Am J Sci*, *301*(2), 150-181. doi: 10.2475/ajs.301.2.150